Accepted to AJ: January 15, 2013
Preprint typeset using LaTeX style emulateapj v. 5/2/11

arXiv:1301.6170v1 [astro-ph.CO] 25 Jan 2013

PROPERTIES OF M31. II: A CEPHEID DISK SAMPLE DERIVED FROM THE FIRST YEAR OF PS1 PANDROMEDA DATA

Mihael Kodric[1,2], Arno Riffeser[1,2], Ulrich Hopp[1,2], Stella Seitz[1,2], Johannes Koppenhoefer[1,2], Ralf Bender[2,1], Claus Goessl[1,2], Jan Snigula[2,1], Chien-Hsiu Lee[3,1], Chow-Choong Ngeow[3], K. C. Chambers[4], E. A. Magnier[4], P. A. Price[4], W. S. Burgett[4], K. W. Hodapp[4], N. Kaiser[4], R.-P. Kudritzki[4]

Accepted to AJ: *January 15, 2013*

ABSTRACT

We present a sample of Cepheid variable stars towards M31 based on the first year of regular M31 observations of the PS1 survey in the $r_{\rm P1}$ and $i_{\rm P1}$ filters. We describe the selection procedure for Cepheid variable stars from the overall variable source sample and develop an automatic classification scheme using Fourier decomposition and the location of the instability strip. We find 1440 fundamental mode (classical δ) Cep stars, 126 Cepheids in the first overtone mode, and 147 belonging to the Population II types. 296 Cepheids could not be assigned to one of these classes and 354 Cepheids were found in other surveys. These 2009 Cepheids constitute the largest Cepheid sample in M31 known so far and the full catalog is presented in this paper. We briefly describe the properties of our sample in its spatial distribution throughout the M31 galaxy, in its age properties, and we derive an apparent period-luminosity relation (PLR) in our two bands. The Population I Cepheids nicely follow the dust pattern of the M31 disk, whereas the 147 Type II Cepheids are distributed throughout the halo of M31. We outline the time evolution of the star formation in the major ring found previously and find an age gradient. A comparison of our PLR to previous results indicates a curvature term in the PLR.

Subject headings: Catalogs – distance scale – Galaxies: individual (M31, NGC 224) – Galaxies: star formation – Local Group – Stars: variables: Cepheids

1. INTRODUCTION

Classical δ Cep variable stars are young massive stars of Population I in their post main sequence evolution. Due to their period-luminosity relation (Leavitt 1908 and Leavitt & Pickering 1912), they are the anchor of the extragalactic distance scale. As such, they are a central topic of many investigations in nearby galaxies (see e.g. Freedman et al. 2001, for a historical summary including the early HST projects, more recent work is discussed e.g. by Riess et al. 2011 and Gerke et al. 2011). δ Cep stars can provide distance estimates out to several 10 Mpc (e.g. Riess et al. 2011), but the major uncertainty of these distance values is still related to the local calibration which until recently totally rested on the LMC distance. As there is an ongoing and unsolved debate to which extent the period-luminosity relation (PLR) of δ Cep stars depends on stellar properties like e.g. the metallicity (Majaess et al. 2011), the LMC is not an optimal choice given its significantly reduced metallicity compared to the large spirals to which the PLR is normally applied. Majaess et al. (2011) summarize the recent discussion with the conclusion that the period Wesenheit (Madore 1976, Madore 1982, Opolski 1983) relation (from colors V and I) does not depend on metallicity while Shappee & Stanek (2011), based on a large sample of δ Cepheid stars observed with HST in two fields of the spiral galaxy M 101, conclude the opposite and in addition report supporting evidence from other studies (Gerke et al. 2011). On the theoretical side there have been predictions that the Wesenheit PLR should depend on metallicity if based on photometric bands sensitive to metal line blanketing (like the combination of Johnson B and V) while the red band combinations of the Johnson-Cousins system should not show this dependence (Fiorentino et al. 2007). The discussion of the PLR properties - in individual photometric bands - has become even more complicated as some authors reported a non-universal slope for the PLR (see Sandage & Tammann 2008 and references therein), which has not been confirmed by others and still is under debate.

The recent discussion on the calibration of the cosmological distance scale and the subsequent determination of the Hubble constant has somehow shadowed that these relatively young and massive stars can be also used as excellent tracers of the recent evolution of stellar populations as they allow number counts in precisely known time bins.

The LMC has been the historical place for the establishment of the PLR (Leavitt & Pickering 1912) as it is close by and can be well resolved from the ground while already distant enough that the member stars are essentially at the same distance. Thus, the LMC (and SMC) were intensively studied for variable stars and transient phenomena by various projects yielding also extensive and well observed samples of Cepheid stars in fundamental, first and second overtone pulsation as well as Population II pulsators (W Vir, RV Tau etc). The most prominent example is probably the OGLE project which provided a well established PLR based on B, V, and I observations of ~ 3400 δ Cep stars in LMC and SMC (Udalski et al. 1999a,Udalski et al. 1999b,Udalski et al. 1999c).

[1] University Observatory Munich, Scheinerstrasse 1, 81679 Munich, Germany
[2] Max Planck Institute for Extraterrestrial Physics, Giessenbachstrasse, 85748 Garching, Germany
[3] Graduate Institute of Astronomy, National Central University, Jhongli City, 32001, Taiwan
[4] Institute for Astronomy, University of Hawaii at Manoa, Honolulu, HI 96822, USA

The nearest example of a Cepheid population in a typical large spiral galaxy of roughly solar metallicity and outside our own Milky Way galaxy is the one in the Andromeda galaxy M31. The first detections go back to Hubble (1929). Baade & Swope (1965) summarize the early observational results which already comprised a sample size of ~ 260 Cepheid variables.

Wide field CCD imagers time series studies brought M31 again into the focus of several projects aiming to detect and study transients and variables stars (e.g. Macri 2004, the DIRECT project; Fliri et al. 2006, Vilardell et al. 2007).

The Fliri et al. (2006) sample (based on the WeCAPP micro lensing project (Riffeser et al. 2001) was observed over almost 8 years with ground based CCD imaging centered on the M31 bulge. Therefore, the δ Cep stars as typical Population I objects are only a minor contribution (33) to the total sample of variable stars and they are even outnumbered by other types of Cepheids (93).

The Vilardell et al. (2007) sample was obtained from observations covering the north-west quarter of the M31 disk. Spanning almost 5 years, the ~ 250 observations in B and V allowed to obtain a sample of 416 Cepheid stars, to study their light curves in detail and to derive distance estimates to M31. A shortcoming of the DIRECT data is that the 250 individual observations were obtained in 21 nights only. The window function (inherent to the observations) implies a strong bias against finding objects within certain period ranges. This can distort results like e.g. the period-number distribution of the sample.

Ground-based M31 observations have been supplemented with single epoch high resolution HST-imaging (PHAT, Johnson et al. 2012), especially in the NIR. This allowed to improve on some of the short-comings of ground-based data for this galaxy and paved the way for a precise distance determination of M31 (Riess et al. 2012).

In this paper we expand the studies of the Cepheid population in M31 with our wide field ground based data taken within the first year of the Pan-STARRS 1 project (Kaiser et al. 2002). Among others, the two major advantages of our data are that, firstly, they cover the complete M31 disk, and, secondly, they are much more evenly distributed in time using observations taken in up to 102 nights ($\sim 80\%$ of the nights have two epochs, giving a total of 183 epochs).

Throughout this paper we will refer to Fundamental mode (FM) Cepheids (classical δ Cep variable stars), First overtone (FO) Cepheids (classical δ Cep variable stars pulsating in the excited mode of the first overtone), Type II Cepheids (W Virginis) and use the term Cepheids for all three subgroups. BL Herculi stars are too faint to be detected with our survey and RV Tauri are excluded manually (c.f. Section 3), so that our Type II Cepheids only consist of W Virginis stars.

This paper is organized as follows: In Section 2 we present the PAndromeda survey, our observations in 2010 and 2011, and a description of our data reduction, including the determination of the light curves for the resolved sources. Our period determination is described in Section 3. The Cepheids detected in the PAndromeda data-set are presented in Section 4. This Section also describes the automatic Cepheid detection and classification. An overview of the catalog is shown in Section 5. We discuss our results, such as (among others) the PLR, the spatial distribution of the Cepheids and the spatial age distribution, in Section 6. We conclude the paper in Section 7.

2. OBSERVATIONS & DATA REDUCTION

2.1. *PAndromeda*

The 1.8 m Panoramic Survey Telescope and Rapid Response System (Pan-STARRS, Hodapp et al. 2004, Kaiser et al. 2002) on Haleakala, Maui, began its regular survey in spring 2010. Pan-STARRS 1 (PS1) uses the Giga Pixel Camera (GPC, Tonry & Onaka 2009) which is currently one of the largest cameras in the world. It consists of 60 OTAs (orthogonal transfer arrays), each of them segmented into an array of 8×8 cells. The total number of pixels is $1.4 \cdot 10^9$, with a pixel size of 0.258 arcsec. The FOV of one OTA is $21' \times 21'$. The aims of PS1 are to map 3π of the sky in $g_{\rm P1}$, $r_{\rm P1}$, $i_{\rm P1}$, $z_{\rm P1}$, $y_{\rm P1}$ bands. In addition to the large 3π area some fields are visited more frequently and have deeper exposure times. One of these so called medium deep fields targets the Andromeda galaxy (M31). With the $\sim$7 deg^2 field of view of Pan-STARRS, a complete monitoring of the disk and large parts of the halo is possible with one single exposure. The PAndromeda survey observes M31 for 0.5 h per night (including overhead) during a period of 5 months per year, equivalent to 2% of the overall PS1 time. We split the integration time into two visits per night (separated by $3\,\mathrm{h} \pm 0.5\,\mathrm{h}$), for the whole season[5]. During the first two seasons we focused on the filters $r_{\rm P1}$ and $i_{\rm P1}$ (Tonry et al. 2012). Observing M31 two times per night with the $r_{\rm P1}$ and $i_{\rm P1}$ filters is a consequence of the PAndromeda survey goal to find microlensing events as described in Lee et al. (2012).

In the first season PAndromeda monitored M31 from 2010-07-23 to 2011-12-27. In this work we used in addition part of the second season from 2011-07-25 to 2011-08-12. This results in a gap of about half a year in the light curves and gives us a total of 183 epochs[6].

2.2. *Data reduction*

The details of the data reduction for PAndromeda are described in Lee et al. (2012). In the following section we summarize the data reduction steps and point out differences to the approach taken in this work.

The GPC1 exposures are de-biased, flat-fielded, and astrometrically calibrated using the Pan-STARRS Image Processing Pipeline (IPP; Magnier 2006). During this process the images are remapped to a common grid, the so called skycells. These warped images have a pixel scale of 0.200 arcsec/pixel, which is smaller than the natural pixel size of

---

[5] Per visit 7 exposures of 60 s in the $r_{\rm P1}$ band and 5 exposures of 60 s in the $i_{\rm P1}$ band are taken. The total integration time per night is therefore 1440 s. The remaining time is spent on readout, focusing and filter change.

[6] Due to masking the total number of epochs for a light curve can be less than 183.

the GPC1 (0.258 arcsec/pixel). For better data management we integrated our pipeline (Koppenhoefer et al. 2011) into the AstroWISE data management system (Valentijn et al. 2007).
In this work we use only data from 24 skycells, namely 039-041, 051-054, 064-068, 076-079, 088-092, 102-104. As shown in Fig. 2.2, the skycell layout is not optimized in the sense that it does not follow the detector boundaries. We plan to optimize the skycell layout and use an intrinsic pixel scale close to 0.258 arcsec/pixel in the future. The following data reduction steps are applied to each skycell and both filters $r_{\rm P1}$ and $i_{\rm P1}$.

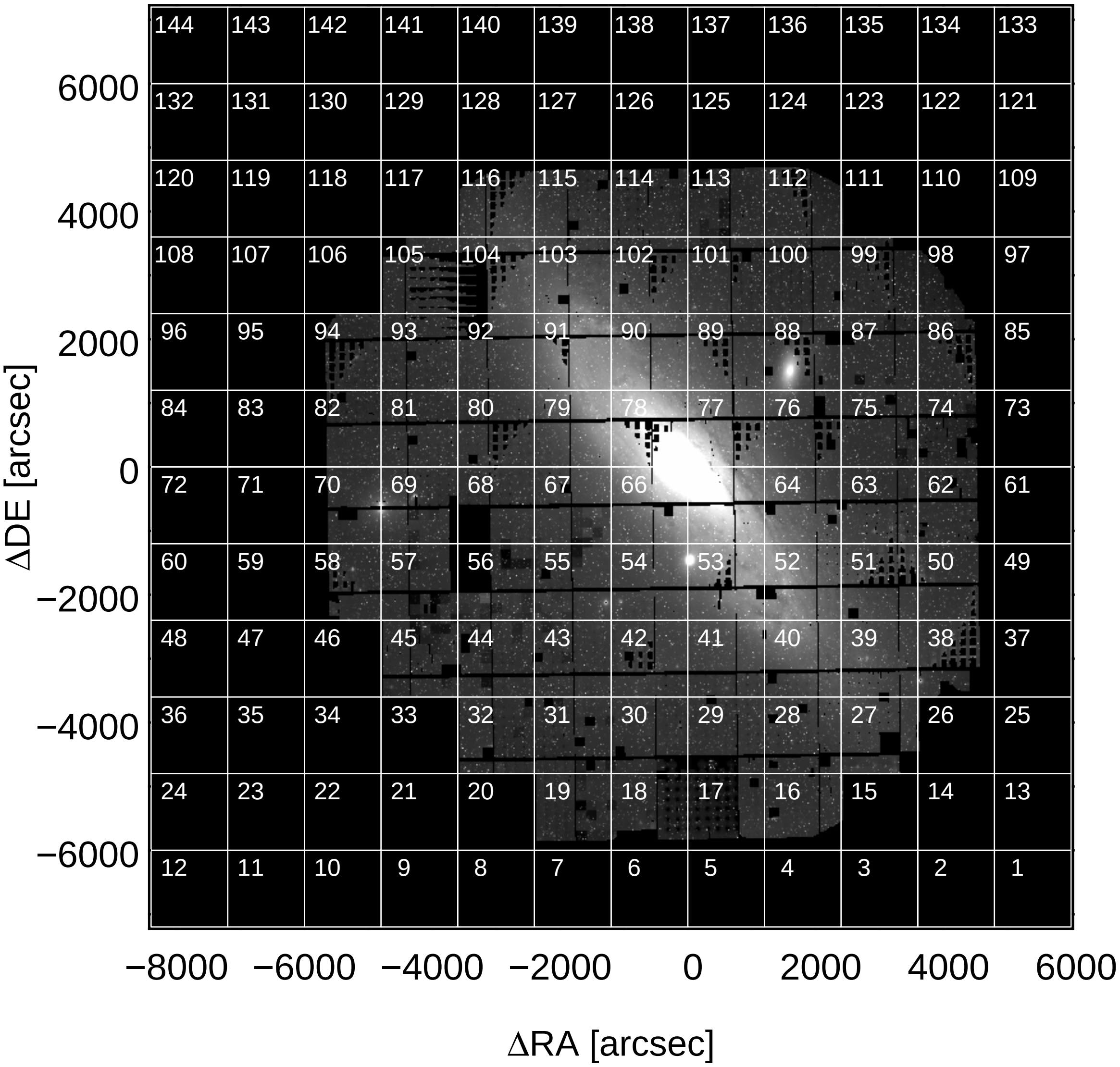

FIG. 1.— Skycell layout for the first season. As can be seen the entire disk of the Andromeda galaxy, M 32 and NGC 205 can be imaged with one pointing. The underlying M31 image is a single $r_{\rm P1}$-band frame, which was chosen to have relatively small masked area. The masked areas (in black) are e.g ill-functioning chips, video guide star cells and areas on the focal plane with sub-standard imaging performance.

Since we use difference image photometry (Tomaney & Crotts 1996), we have to produce a stack of images with the best seeing, the so called reference image. We photometrically align the 70 best seeing images, so that the images have the same zero point and the same (non zero) sky background. In the next step we replace masked areas in the photometrically aligned images with values from another image that has the most similar PSF (Riffeser 2006, p. 134). The weighted stack of the aligned images is called the reference image.
We use SExtractor to detect sources on the reference image (Bertin & Arnouts 1996). For the data utilized in this work, SExtractor is used in a mode that modifies the detection threshold depending on the background. While this mode is very useful it hampers completeness tests.
For all sources in the reference image, we perform PSF photometry on a background (sky and M31) subtracted reference image. In order to obtain the background in the reference image, we fit a bicubic spline model. To suppress blending effects we iteratively subtract neighboring stars. The fluxes measured in the reference image are added later to the fluxes in the difference images, so as to create the light curves. The flux error in the reference image determined by the PSF photometry does not take into account how well our constant PSF model matches the real sources in the

reference frame which can show slight PSF-variation over the field. This can result in wrong flux errors. To obtain reasonable errors we rescale the error of each source with the $\sqrt{\chi^2}$ of its PSF fit.

To minimize masking and to obtain a better signal-to-noise ratio we stack the images of each visit. The procedure is the same as for the reference images. The visit stacks are photometrically aligned to the reference image, so that the visit stacks and the reference image have the same zero point and sky background. At this point they only deviate in signal-to-noise and PSF-shape.

To create the difference images we first align the PSF of the reference image to match the PSF of the visit stack by calculating a constant convolution kernel by least-squares minimization from all pixels in subareas of $75'' \times 75''$ (see Alard & Lupton 1998). This PSF aligned reference image is then subtracted from the visit stack. On this difference image we perform PSF photometry to obtain light curves. The PSF is constructed with sub-pixel precision from the convolved reference image using isolated stars. Since we only measure the flux difference we add the flux measured in the reference image to this flux difference to obtain the light curves for the resolved sources. Fig. 2 summarizes the PAndromeda data reduction pipeline.

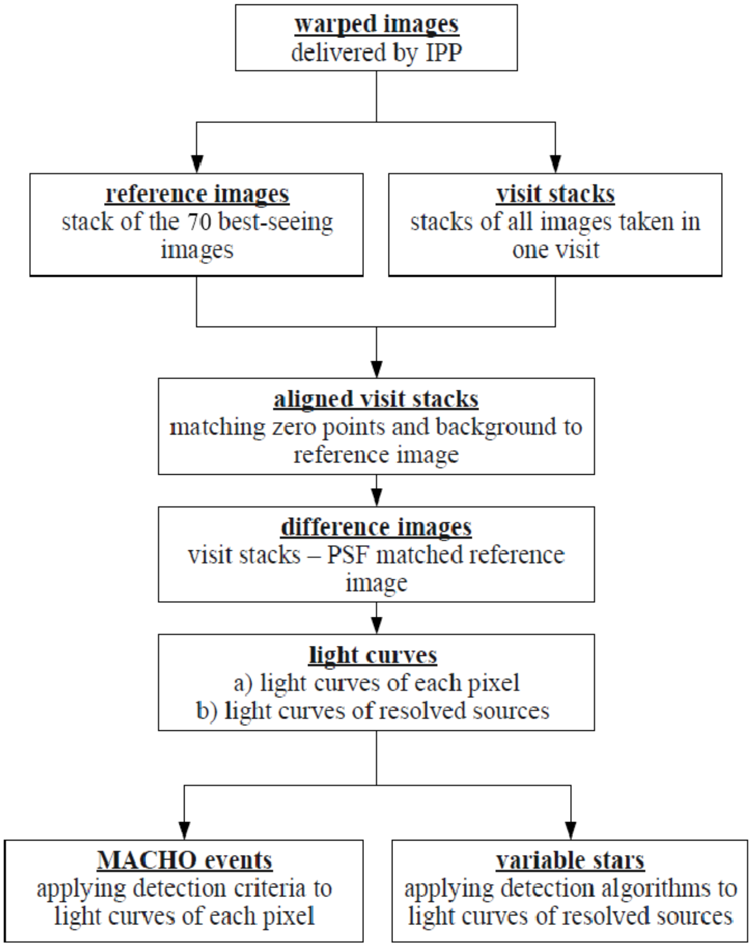
warped images
delivered by IPP
reference images
stack of the 70 best-seeing images
visit stacks
stacks of all images taken in one visit
aligned visit stacks
matching zero points and background to reference image
difference images
visit stacks – PSF matched reference image
light curves
a) light curves of each pixel
b) light curves of resolved sources
MACHO events
applying detection criteria to light curves of each pixel
variable stars
applying detection algorithms to light curves of resolved sources

Fig. 2.— Summary of the PAndromeda data reduction pipeline (taken from Lee et al. 2012 (modified)). We use 70 images for the reference image stacking, instead of the 30 that Lee et al. (2012) use.

Note that the astrometric precision and photometric stability have been discussed in Lee et al. (2012). For the flux calibration we make use of the fact, that the r_{P1} and i_{P1} bands are rather similar to the Sloan Digital Sky Survey (SDSS; Abazajian et al. 2009) r_{SDSS} and i_{SDSS} bands and thus the flux calibration should be insensitive to color terms (Tonry et al. 2012). To calibrate our magnitude to the SDSS magnitude system with stars from SDSS we use:

$$m_{\mathrm{SDSS}} = -2.5\log\left[F_{\mathrm{ref}}(\mathrm{PSF}_{\mathrm{ref}}) + \Delta F_{\mathrm{diff}}(\mathrm{PSF}_{\mathrm{diff}}) + \mathrm{ZP}_{\mathrm{PSF}}\right] \tag{1}$$

$F_{\mathrm{ref}}(\mathrm{PSF}_{\mathrm{ref}})$ is the flux of a source determined by PSF photometry in the reference image and $\Delta F_{\mathrm{diff}}(\mathrm{PSF}_{\mathrm{diff}})$ the flux determined by PSF photometry in the difference image. $\mathrm{ZP}_{\mathrm{PSF}}$ accounts for the difference between SDSS magnitudes and our instrumental magnitudes and does also consider the PSF construction.

Our pipeline does not take into account the correlated noise that arises from the change of the pixel scale. To quantify this we constructed light curves of all pixels, normalize each single deviation from the fitted mean by its error. The distribution of these normalized deviations is clearly dominated by the non-varying pixels. Then the correction factor can easily be estimated by comparing this distribution with a standard Gaussian-distribution (sig = 1). This rescaling factor is the same for every skycell and filter.

Throughout this paper, we will use the AB magnitude system.

3. PERIOD DETERMINATION

The periodicity of the light curves is determined with the software `SigSpec` (Reegen 2007). `SigSpec` calculates a quantity called *spectral significance* (sig) for each peak in the discrete Fourier transform (DFT) amplitude spectrum of a light curve. Similar to the false alarm probability[7] $\Phi_{\rm FA}(A)$

$$\mathrm{sig}(A) := -\log\left[\Phi_{\rm FA}(A)\right] \tag{2}$$

is a measure for the probability that a peak arises from noise. This value does not only depend on the amplitude and frequency, but also on the phase and the sampling of the light curve. This fact gives `SigSpec` an advantage over the use of other Fourier based algorithms such as the Lomb-Scargle algorithm (Lomb 1976, Scargle 1982). While both methods produce comparable results concerning the period, we found that `SigSpec` finds more periodic light curves over a given false alarm probability threshold than the Lomb-Scargle algorithm. This is due to the fact that certain periods have to be excluded in the Lomb-Scargle algorithm, depending on the sampling of the light curve in order to avoid aliasing.

In the following paragraph we outline the parameters with which we run `SigSpec`. As statistical weight we use the inverse variance ($w_i = \sigma_i^{-2}$) of the PSF flux measurement and we use [JD − 2450000] for the epoch. We apply a sig-threshold of 5 (`siglimit 5`) to determine the periodicity of the light curves. This means that in less than one out of 10^5 cases pure noise could produce the measured period. With a lower threshold the number of detections would increase (e.g. by a factor of ~ 10 with a threshold of 3), but most of the detections would be low signal-to-noise detections. With the parameter `ufreq 1` we define the lowest period to be considered as 1 day. We exclude smaller periods because they can hardly be detected with a sampling of two visits per night. An upper limit for the period has not been defined, but a period cut is performed later on. The last two parameters (`multisine:lock` and `iterations 1`) force `SigSpec` to consider only the most significant peak[8] in the DFT amplitude spectrum ensuring that noise has no impact on the determined period. We use no variability index since `SigSpec` only determines periods for variable sources.

Inspection by eye of the folded light curves, that `SigSpec` detects, showed the good performance in the period determination of `SigSpec`. One problem, however is the lack of an upper period limit that permits `SigSpec` to determine periods even if the signal is not periodic[9]. The inspection showed that for large periods some of the folded light curves look like Cepheid light curves. We did not exclude those light curves at this stage, but rather applied a period cut later on. As our data set also contains 10 days of observations of season 2011, the data show a gap of half a year between these data points and the 2010 data points. In some cases the 2011 data points have a small flux shift from the 2010 data points in the folded light curve. This may have different reasons. Firstly the shift could be due to flux variations. Secondly it could be caused by a small deviation from the true period, which can be observed in the folded light curve if the period is small enough. And lastly the frequency spacing used by `SigSpec` could be too low. Also in the case of RV Tauri variables `SigSpec` detects the wrong period, as it identifies the time span between the primary and secondary minimum as the period. We identified and rejected those light curves manually[10]. From 724894 sources that were detected in the $r_{\rm P1}$ band and which have light curves in the $r_{\rm P1}$ and $i_{\rm P1}$ band[11], `SigSpec` finds 75362 periodic variable light curves with sig > 5.

Since `SigSpec` does not determine the period error, we use the bootstrap method to estimate the period uncertainties. A random sampling is drawn from the light curve (one epoch can be drawn multiple times) and the period for that sampling is determined with `SigSpec` (with a sig-threshold of 1). This procedure is performed 1000 times for each light curve, so that the 1σ error can be determined from the resulting distribution. The obtained period errors for the Cepheids of the 3-dimensional parameter space classified Cepheid catalog (see Section 4.6) are shown in Fig. 3. The classification of the different Cepheid types shown in Fig. 3, as well as the meaning of the 3-dimensional parameter space classified Cepheid catalog, is described in the next section.

In general the period errors are small, except for some light curves where the distribution has an additional peak at ~ 1.5 d due to aliasing. For those light curves the large error is only caused by this additional peak. It is not a broader distribution that causes the larger error and therefore the period error would be small if there is no aliasing. Since we find no aliasing in the final Cepheid light curves and the systematics have a larger effect than the period errors, we disregard the period errors, which means that the period errors shown in the plots do not contribute to any selection criteria or fit.

---

[7] The false alarm probability $\Phi_{\rm FA}(A)$ is the integrated probability density function and describes the probability that an amplitude exceeds a given limit A as described in Reegen (2007).

[8] The `SigSpec` default value would perform an iterative sequence, the so called prewhitening sequence. After the most significant peak is identified, a fit to all signals that are identified so far is performed. This fit is then prewhitend (subtracted) from the spectrum and the next iteration starts until the maximum peak is under the threshold.

[9] `SigSpec` can determine a period for almost every signal that is not constant. If the signal is not periodic and not constant the program usually detects the total observation time as the period.

[10] RV Tauri light curves are rather easy to distinguish from the Cepheid light curves, since the RV Tauri light curves appear as an overlay of two shifted light curves.

[11] We detect the variable sources in the $r_{\rm P1}$ band and therefore there is always a light curve in the $r_{\rm P1}$ band for each variable source. But the same source can be masked in the $i_{\rm P1}$ band so that there is no light curve in the $i_{\rm P1}$ band.

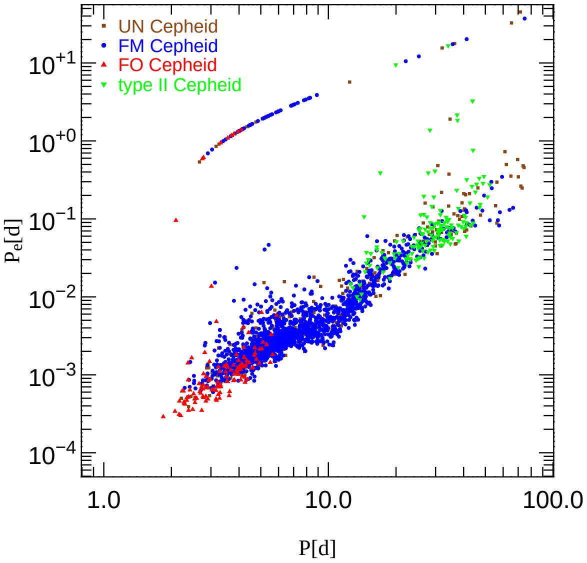

FIG. 3.— Period errors P_e determined through the bootstrap method for the 3-dimensional parameter space classified Cepheid catalog. The large period errors of $P_e \gtrsim 0.5$ days are caused by aliasing produced by $\sim 3.5\%$ of the bootstrap light curves.

4. CEPHEID DETECTION AND CLASSIFICATION

As described in the previous section we narrowed the number of variable sources down to those that have periodic light curves. In this sample of variable sources we want to identify the Cepheids.

The classical approach to find the Cepheids (e.g. Udalski et al. 1999a, Vilardell et al. 2007) is to preselect sources in a certain brightness and color range and to visually inspect them. But the position of the instability strip spans an area depending on brightness and color (Fiorentino et al. 2002 and Marigo et al. 2008, including the updates by Girardi et al. 2010) and is incorrectly described by a rectangle in the color-magnitude diagram (see Fig. 4.2). For our color cut we therefore use the instability strip of the Cepheids translated into our filter system (Fiorentino et al. 2002, Marigo et al. 2008, Girardi et al. 2010). We choose a different approach than the visual inspection and establish an automatic Cepheid detection. The motivation for this is that the selection based purely on light curves is always biased, in particular if the light curves become more noisy. We define limits in a 3-dimensional parameter space which define our Cepheids. In order to define the parameter space we select a subsample of the periodic light curves and visually select the Cepheids. The manual selection is of course also biased, but the advantage of this method is that the selection of the remaining Cepheids only depends on the defined parameter space. The parameters used are derived from a Fourier decomposition of the light curves. With this method we were also able to identify the Cepheid type. The fundamental mode Cepheids and the first overtone Cepheids can be distinguished this way as e.g. shown by Udalski et al. (1999a) and Vilardell et al. (2007). We can additionally also distinguish the Type II Cepheids from the other two mentioned Cepheid types.

Additionally we impose certain requirements on the remaining variable sources detected by `SigSpec`, so as to exclude bad light curves.

In the following Sections we describe our approach that we outlined here.

4.1. *Fourier decomposition*

A Fourier decomposition of the folded light curves can be used to distinguish between fundamental mode (FM) Cepheids and first overtone (FO) Cepheids (Udalski et al. 1999a, Vilardell et al. 2006). We also use Fourier decomposition to identify Type II Cepheids and to define the 3-dimensional parameter space in which we detect the Cepheids.

We fit a Fourier series to the light curve of the form

$$m(t) = a_0 + \sum_{n=-N}^{-1} a_n \cdot \cos(n\omega t) + \sum_{n=1}^{N} a_n \cdot \sin(n\omega t) \tag{3}$$

with P being the period of the light curve determined by `SigSpec`), $\omega = \frac{2\pi}{P}$ and $t \in [0, P]$. Prior to the fit we convert the flux to magnitudes and fold the light curves, so that they show the variation of the magnitude over the phase θ times the period[12] P. With this fit we determine the minimum and maximum of the light curve and the coefficients a_n. We also calculate the magnitude of the mean flux, needed later for the PLR. This is different to a mean magnitude, which we would get if we take the mean of the light curve. For this reason we transform the Fourier series fit back to flux and calculate the mean flux and then convert this to a mean magnitude.

---

[12] That is why $t \in [0, P]$ and not $t \in [0, 1]$, what would be the case for folded light curves that vary over the phase.

For an analysis of the Fourier decomposition we transform the Fourier series to the form:

$$m(t) = b_0 + \sum_{k=1}^{N} b_k \cdot \cos(k\omega t + \varphi_k) \tag{4}$$

with $b_k = \sqrt{a_{-k}^2 + a_k^2}$ and $\varphi_k = \arctan \frac{-a_k}{a_{-k}}$. This allows us to calculate the amplitude ratio

$$A_{21} \equiv \frac{b_2}{b_1} \tag{5}$$

and the phase difference

$$\varphi_{21} \equiv \varphi_2 - 2 \cdot \varphi_1 \tag{6}$$

for each light curve (Vilardell et al. 2007). The period P and the coefficients A_{21} and φ_{21} are used to define the 3-dimensional parameter space (P, A_{21}, φ_{21}) and to identify the Cepheid type.

We chose $N = 5$ for the Fourier series fit. Other degrees of freedom (d.o.f.) would result in slightly different amplitudes a_n. In most cases the deviations of the a_n from other d.o.f., compared to the a_n of $N = 5$, is small, but there are also light curves with significant deviations for higher d.o.f.. While $N = 5$ is sufficient to fit bumps (c.f. left panel Fig. 12) in the light curves, higher d.o.f. are more susceptible to 'overshoots' and tend to be more influenced by outliers. This is why we do not determine the optimal d.o.f. for each light curve as e.g. described in Deb & Singh (2009). The principal component analysis (PCA) technique demonstrated in Deb & Singh (2009) does not offer any advantage in the form of saving computation time, since we use a linear least squares fit and not a non linear fit for which the PCA is faster.

Additionally we derive a polynomial fit with two boundary conditions of the form:

$$p(t) = a_0 + \sum_{n=1}^{K} a_n t^n \quad \text{with} \quad p(0) = p(P) \ \wedge \ p'(0) = p'(P) \ \wedge \ t \in [0, P] \tag{7}$$

to the folded light curves (in magnitudes). For this fit a change in the number of d.o.f. also changes the a_n, so we chose $K = 10$ in order to have the same number of d.o.f. as in the Fourier series fit. With this polynomial fit we have an alternative light curve description to the Fourier series. The best fitting Fourier and polynomial fits are affected by data gaps in a different way and they produce different 'overshoots'. We compare the Fourier and polynomial fits to identify and exclude badly fitted light curves, as we will describe in the next section.

4.2. *Wesenheit-color cuts*

Young stars are located in spiral arms which are also populated by interstellar dust. The dust in the arms show a clumpy distribution and Cepheids may be either located before, within, or behind this dust.

Although Population II Cepheids are not located in the M31 disk it is not a priori known whether they stay in front of or behind the disk. Therefore, even for the majority of the Population II objects an understanding of the internal reddening is required for each single object.

As already mentioned the preselection of sources in a certain brightness and color range depends on the instability strip. But it also depends on the reddening. By using the Wesenheit magnitude the brightness is independent of reddening and only the color is affected by extinction. For this reason we use the Wesenheit-color plane and select Cepheids according to the location of the instability strip.

The Wesenheit magnitude is defined to be independent of reddening (Madore 1976, Madore 1982, Opolski 1983)

$$W = r_{\mathrm{P1}} - R(r_{\mathrm{P1}} - i_{\mathrm{P1}}) = r_{\mathrm{P1},0} - R(r_{\mathrm{P1},0} - i_{\mathrm{P1},0}). \tag{8}$$

With $r_{\mathrm{P1}} = r_{\mathrm{P1},0} + A_{r_{\mathrm{P1}}}$, $i_{\mathrm{P1}} = i_{\mathrm{P1},0} + A_{i_{\mathrm{P1}}}$ and $A_{r_{\mathrm{P1}}}$ and $A_{i_{\mathrm{P1}}}$ being the extinction corrections in the r_{P1} and i_{P1} bands we can derive the coefficient:

$$\begin{aligned} & r_{\mathrm{P1},0} + A_{r_{\mathrm{P1}}} - R(r_{\mathrm{P1},0} - i_{\mathrm{P1},0}) - R(A_{r_{\mathrm{P1}}} - A_{i_{\mathrm{P1}}}) = r_{\mathrm{P1},0} - R(r_{\mathrm{P1},0} - i_{\mathrm{P1},0}) \\ & \Rightarrow R = \frac{A_{r_{\mathrm{P1}}}}{A_{r_{\mathrm{P1}}} - A_{i_{\mathrm{P1}}}} \end{aligned} \tag{9}$$

The galactic extinction coefficients $\frac{A_{r_{\mathrm{P1}}}}{E(B-V)}$ and $\frac{A_{i_{\mathrm{P1}}}}{E(B-V)}$ are (Tonry et al. 2012):

$$\begin{aligned} \frac{A_{r_{\mathrm{P1}}}}{E(B-V)} &= 2.585 - 0.0315 \cdot (g_{\mathrm{P1},0} - i_{\mathrm{P1},0}) \\ \frac{A_{i_{\mathrm{P1}}}}{E(B-V)} &= 1.908 - 0.0152 \cdot (g_{\mathrm{P1},0} - i_{\mathrm{P1},0}) \end{aligned} \tag{10}$$

Fiorentino et al. (2002) provides the position of the instability strip for Cepheids depending on $\frac{L}{L_\odot}$ and T_{eff} ($L_\odot$ is the solar luminosity and T_{eff} the effective Temperature). We combine this with the isocrones from Marigo et al. (2008) with the corrections by Girardi et al. (2010) with $Z = 0.019$, for different $\frac{L}{L_\odot}$ and T_{eff}, thus allowing us to determine the theoretical location of the Cepheids in the color-magnitude diagram, as shown in the left panel of Fig. 4.2. The

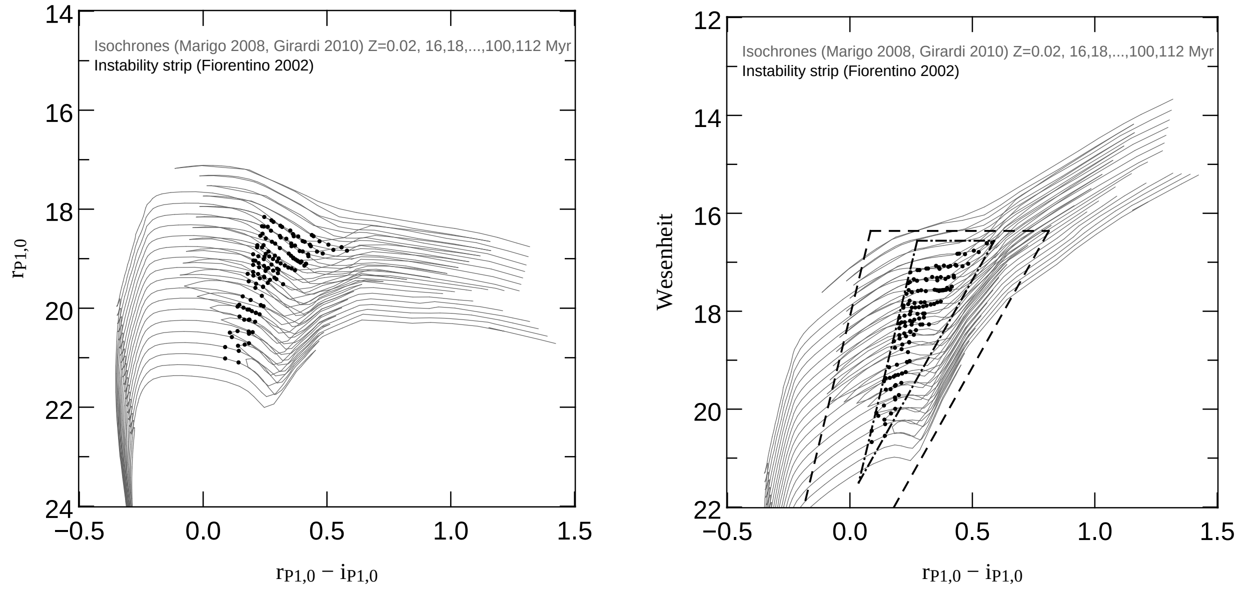

FIG. 4.— Domain of the instability strip for Cepheids used for the Wesenheit-color cut. A distance modulus of 24.36 (Vilardell et al. 2010) has been applied to the magnitudes. Left panel: Location of the instability strip for Cepheids in the magnitude-color plane according to instability theory. Right panel: Location of the instability strip for Cepheids in the Wesenheit-color plane according to instability theory. The area inside the dashdotted lines encloses the instability strip and the area within the dashed lines is where we require the mean magnitude of the light curve to be in, within their error margin. To define this domain we enlarged the boundaries of the dashdotted region by 0.2 *mag* in both color directions and by 0.2 *mag* in direction of brighter Wesenheit magnitudes.

right panel of Fig. 4.2 shows the domain defined by this theoretical prediction in the color-Wesenheit diagram (defined by a triangle with the corners (0.036/21.50), (0.275/16.56) and (0.59/16.56)). A candidate is qualified as a Cepheid variable star if its mean magnitude is located inside this triangle (including its 1σ error). Similar to Fig. 4.2 we also obtained the location of the Cepheids in the $g_{\rm P1,0}$ vs. $g_{\rm P1,0} - i_{\rm P1,0}$ plane, see Fig. 5. For $(g_{\rm P1,0} - i_{\rm P1,0}) = 1.0$ and from Eq. 10 we get $\frac{A_{r_{\rm P1}}}{E(B-V)} = 2.5535$, $\frac{A_{i_{\rm P1}}}{E(B-V)} = 1.8928$ and $R = 3.86$. Since the $(g_{\rm P1,0} - i_{\rm P1,0})$ correction is small, the min-max error in R is $\Delta R = 0.04$, which makes $(g_{\rm P1,0} - i_{\rm P1,0}) = 1.0$ a reasonable choice.

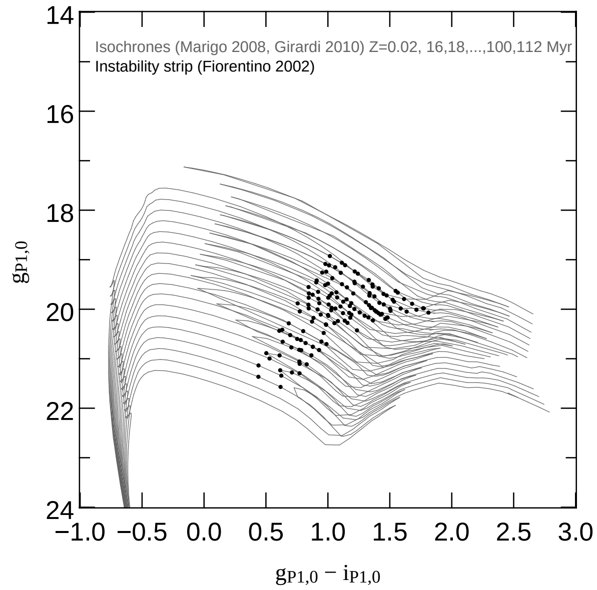

FIG. 5.— Domain of the instability strip for Cepheids used to determine the $(g_{\rm P1,0} - i_{\rm P1,0})$ correction in the galactic extinction coefficients. Since the correction is small, $(g_{\rm P1,0} - i_{\rm P1,0}) = 1.0$ is a reasonable choice.

While the Wesenheit magnitude is independent of extinction, the color is not. Therefore we apply an extinction correction to the colors. We use the $E(B-V)$ map from Montalto et al. (2009) and the foreground extinction of M31 derived by Schlegel et al. (1998) with $E_{\rm fg}(B-V) = 0.062$ and apply the recalibration factor of 0.86 (Schlafly & Finkbeiner

2011), to determine a mean extinction for each light curve depending on its (projected) position:

$$\overline{A_{r_{\rm P1}}} = \frac{E(B-V) + 0.86 \cdot 0.062}{2} \cdot \frac{A_{r_{\rm P1}}}{E(B-V)} \tag{11}$$

$$\overline{A_{i_{\rm P1}}} = \frac{E(B-V) + 0.86 \cdot 0.062}{2} \cdot \frac{A_{i_{\rm P1}}}{E(B-V)} \tag{12}$$

Note that for Cepheids that are outside the Montalto et al. map we only corrected for the foreground extinction. Obviously we could use an extinction corrected magnitude and use it instead of the Wesenheit, but since the correction is associated with a large systematic uncertainty it is better to use the Wesenheit, which does not require an extinction correction. The Wesenheit thus has a higher statistical error, but a lower systematic error relative to the extinction corrected magnitudes.

With the Wesenheit and the extinction corrected $(r_{\rm P1,0} - i_{\rm P1,0})$ color we are able to select only those light curves belonging to the instability strip. This Wesenheit-color, applied to the 75362 periodic light curves detected by `SigSpec`, excludes 70% of the light curves.

4.3. *Manual classification*

In order to find out in which part of the P, A_{21}, φ_{21} 3-dimensional parameter space the Cepheids are located, we need a 'training' set of Cepheids which we obtain from a manual classification, i.e. by visual inspection of the preselected light curves.

The visual inspection of a subsample of Cepheid candidates and admission or rejection of Cepheids based on the light curve can lead to a bias if the Cepheid subsample itself does not represent all Cepheid types. The most unbiased way to select a Cepheid candidate subsample for manual classification is to use the *spectral significance* (sig). On the one hand the significance threshold has to be chosen low enough to contain a fair amount of Cepheids, so that there are enough Cepheids for the exploration of the 3 dimensional parameter space. On the other hand, we do not want the Cepheid candidate subsample to contain so many Cepheids already, that the classification with the parameter space does not detect significantly more Cepheids than the subsample.

For the manual classification we thus selected all light curves that have $sig > 25$ in the $r_{\rm P1}$band. As reference light curves for the manual classification we used the Cepheid light curves from Sterken & Jaschek (2005).

The resulting manual classified subsample contains 1020 Cepheids. This subsample makes up $\sim 50\%$ of the final Cepheid sample.

4.4. *Type classification*

As already mentioned in Section 4.1 the Fourier decomposition can be used to distinguish between FM Cepheids and FO Cepheids. This is done by identifying different locations of the Cepheids in the A_{21}-P and φ_{21}-P planes (e.g. Udalski et al. 1999a, Vilardell et al. 2007). Fig. 6 shows these projections for the manually classified Cepheid catalog. When looking at the Cepheids in a 3-dimensional plot in A_{21}-φ_{21}-P space, it becomes clear that there are indeed three different relatively well separated distributions with only small overlap areas.

The FM Cepheids correspond to the 'V-shaped' sequence that can be seen in in the left panel of Fig. 6. In a 3-dimensional plot the FM sequence appears spiral shaped and the two branches are shifted slightly from one another. The FO Cepheid sequence is perpendicular to the FM sequence, but there is also an overlap regime between them where FM and FO objects can be hardly distinguished. For objects in or near this overlap area the classification into FM or FO is therefore rather uncertain as a real parameter overlap seems to be present.

We additionally find a third sequence not present in Udalski et al. (1999a) and Vilardell et al. (2007) and corresponding to Type II Cepheids. This sequence is more distinct from the FM Cepheids than the FO Cepheids, nevertheless there is also a transition between the two.

In a first step we define the parameter space where most of the FO Cepheids and the Type II Cepheids are located and assign the according type to the Cepheid. We use

$$P < 6.0 \text{ d} \quad \text{and} \quad A_{21} < -0.498 \log(P) + 0.528 \tag{13}$$

for the FO parameter space.

For the Type II space we use

$$11.95 \text{ d} < P < 53.0 \text{ d} \quad \text{and} \quad \varphi_{21} > 5 \text{ rad.} \tag{14}$$

The remaining Cepheids are FM Cepheids. Fig. 6 shows the three different sequences. Nevertheless there are transitions between the sequences. There are FM Cepheids in the FO and Type II parameter space and FO Cepheids or rather Type II Cepheids in the FM sequence. In order to account for these ambiguous cases we identify these Cepheids in a second step by using the Period - Wesenheit relation. By using the Wesenheit and not the $r_{\rm P1}$ band we get a classification independent of reddening. We perform iterative 3σ clipping for a linear relation ($W = a \cdot \log(P) + b$, c.f. Section 6.4) for each Cepheid type and classify all clipped Cepheids and all those Cepheids with a large error in the Wesenheit ($\Delta W > 0.9$) as unclassified (UN) Cepheids. Fig. 7 shows that this classification works well, but also indicates the problem with this approach. Cepheids that are e.g. outside the defined Type II parameter space will be classified as UN Cepheids although it is apparent from Fig. 7 that they are most likely Type II Cepheids.

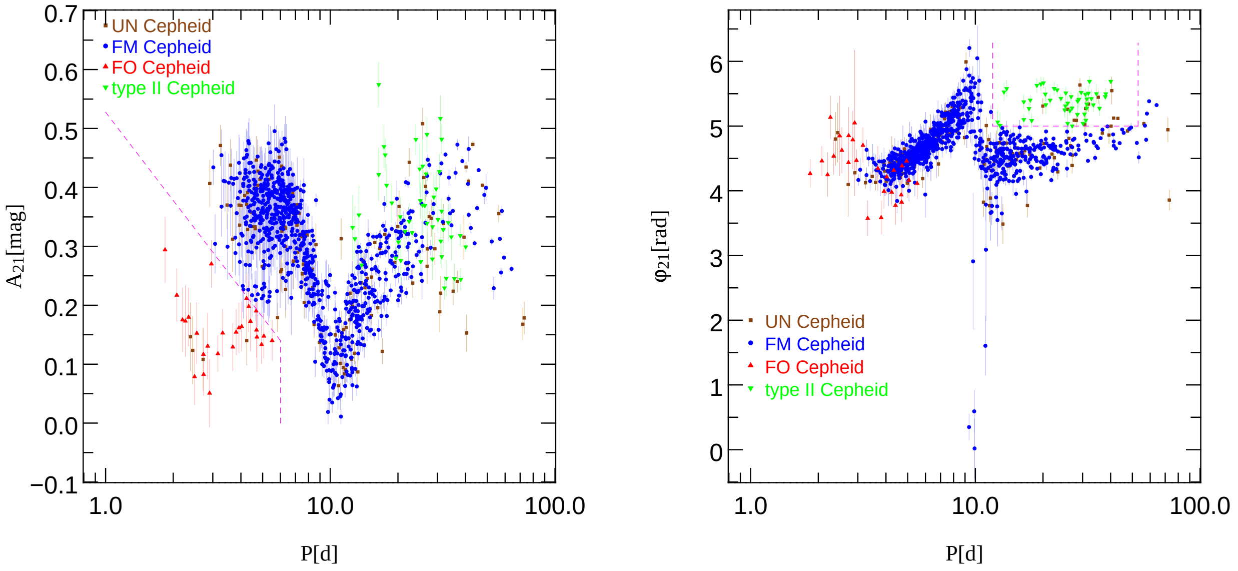

FIG. 6.— 3-dimensional parameter space for the manually classified Cepheid catalog in the $r_{\rm P1}$ band. The scope defined by the magenta dashed lines defines the parameter space in which most of the FO Cepheids ($P < 6.0\,\rm d$ and $A_{21} < -0.498289 * log(P) + 0.527744$) or rather most of the Type II Cepheids ($11.95\,\rm d < P < 53.0\,\rm d$ and $\varphi_{21} > 5\,\rm rad$) reside in, while the FM Cepheids occupy the remaining parameter space. Since there are transitions between the different scopes, we perform a 3σ clipping in the Period - Wesenheit relation (cf. Fig. 7) for each Cepheid type. All the clipped Cepheids and all those Cepheids with a large error in the Wesenheit ($\Delta W > 0.9$) are classified as unclassified (UN) Cepheids. Left panel: Amplitude ratio A_{21} in the $r_{\rm P1}$band. Right panel: Phase difference φ_{21} in the $r_{\rm P1}$band.

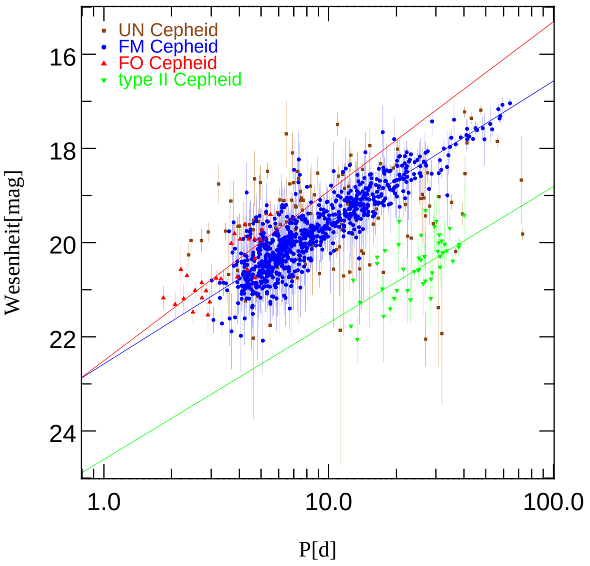

FIG. 7.— Period - Wesenheit relation for the manually classified Cepheid catalog. The Period - Wesenheit relation is used to identify those Cepheids that reside between the type classification scopes (cf. Fig. 6). This is done by performing 3σ clipping for a linear relation ($W = a \cdot log(P) + b$, c.f. Section 6.4) for each Cepheid type (FM Cepheids: blue symbols and line; FO Cepheids: red symbols and line; Type II Cepheids: green symbols and line). All the clipped Cepheids and all those Cepheids with a large error in the Wesenheit ($\Delta W > 0.9$) are classified as unclassified (UN) Cepheids.

4.5. *Selection criteria*

With a visual inspection of the light curves only a color cut is needed to identify the Cepheids. Since we want to identify Cepheids using the P, A_{21}, φ_{21} 3-dimensional parameter space cut we have to apply additional selection criteria to exclude bad light curves. Note that the following criteria can be applied in any order. Table 1 summarizes the selection cuts.

The first two criteria (I & II) concern the period of the light curve. As already mentioned in Section 3 we have not applied a period cut yet. Our data covers approximately 150 days in 2010 and a few days only in 2011. While inspecting the light curves by eye, these few days in 2011 can help to confirm that the detected period is valid, even if the period is $\sim 100\,\rm d$. However since there is a gap of approximately half a year between the 2010 and 2011 data with only few days of observations in 2011, the light curve could be irregular in the time span of the gap and the data points in 2011 could fit to the folded light curve by chance. We decided therefore to select only light curves with periods below 75 days (I) , so that the whole period cycle is sampled at least twice in the 2010 data. We note that there could very well be Cepheids with larger periods than that, but we will be able to confirm those only after the release of the full 2011 data. The second criterion (II) is that the period determined in the $i_{\rm P1}$ filter differs from that in the $r_{\rm P1}$ filter by less than one percent. This criterion excludes most of the light curves (84 %).

We do not require a light curve to contain more than a certain number of epochs. The reason for this is that we use the Fourier series fit and the polynomial fit to account for gaps in the data that might be problematic and produce 'overshoots'. Most of our light curves have ~ 180 epochs, but there can also be light curves with as few as 60 epochs[13]. The left panel of Fig. 8 shows the distribution of the number of epochs for the 3-dimensional parameter space classified Cepheid catalog. The right panel of Fig. 8 shows that there are only a few Cepheids with a small number of epochs when normalized to the period of the light curve in the 3-dimensional parameter space classified Cepheid catalog. A visual inspection shows that these light curves constitute Cepheids. This indicates that we need no criterion requiring a certain number of epochs when applying the three 'overshoot' criteria (The classification of the different Cepheid types shown in Fig. 8 is described in the next Sections).

The criteria III & IV exclude extreme 'overshoots' by selecting only those light curves, where the magnitudes $m(t)$ of the fitted light curve are reasonable: $m(t) < 30$ mag and $m(t) > 15$ mag.

Note that criteria I to IV are applied to both $r_{\rm P1}$ and $i_{\rm P1}$ band. All other criteria only concern the $r_{\rm P1}$ band.

In order to also exclude less extreme 'overshoots', we apply criterion V, which selects only light curves with similar Fourier series fit and polynomial fit. We check for similarity by calculating the area between both fits and demand that the area $\int\limits_0^P (m(t) - p(t))^2 dt$ is below a threshold. The median of this area is ~ 0.2 mag $\cdot$ d and the largest area is ~ 13 for the 3-dimensional parameter space classified Cepheid catalog. So our threshold of 30 is quite high when compared to those numbers, but the 'overshoots' usually produce orders of magnitude larger values than this threshold. The choice of the threshold is arbitrary to some degree, although the threshold of 30 has proven to work well.

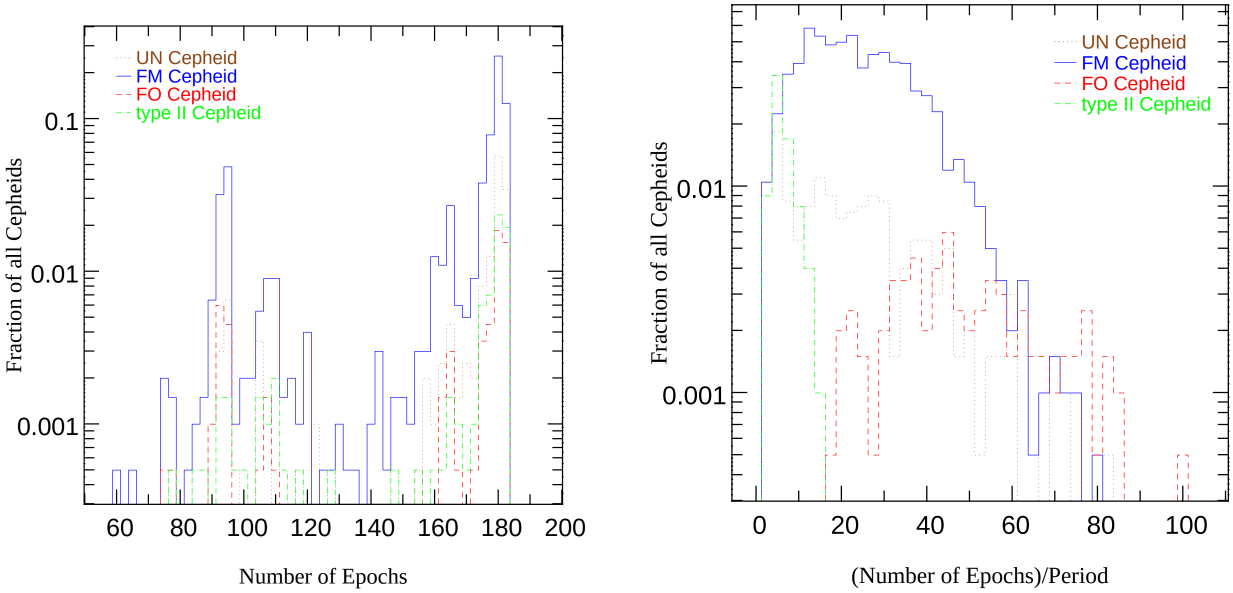

Fig. 8.— Epoch distribution for the 3-dimensional parameter space classified Cepheid catalog in the $r_{\rm P1}$ band. Left panel: Distribution of the number of epochs. Right panel: Distribution of the number of epochs divided by the period.

The last two selection criteria (VI & VII) concern the noise in the folded light curves. If the maximum and minimum of the Fourier series fit are similar, we cannot exclude that the light curve is constant and the variation is caused by noise. Additionally light curves affected by blending have smaller amplitudes. Therefore we select only those light curves with: $\max(m(t)) - \min(m(t)) \geq 0.1$ mag. The χ^2 of a fit can be low, although the scatter is large, if the errors in the data points are large enough. Therefore we introduce a last selection criterion (VII), which concerns the scatter of the light curve. We want to allow for a few points to scatter, that is why we compare the median scatter of the Fourier series fit with the total change in magnitude: $\text{median}\left[|m(t) - y(t)|\right] \leq 0.2\,(\max(m(t)) - \min(m(t)))$ ($m(t)$ is the magnitude of the Fourier series fit at time t and $y(t)$ is the measured magnitude at time t). The threshold of 0.2 was optimized by a visual inspection.

4.6. *3-dimensional parameter space classification*

After the selection criteria are applied (c.f. Section 4.5) we are left with some objects with well defined light curves that are not Cepheids. This becomes obvious if we compare their location in the 3-dimensional parameter space (A_{21}-φ_{21}-P) with that of our manually classified Cepheids. Therefore we use the manually classified subsample to define

---

[13] 60 is the lowest number of epochs for a light curve associated to a Cepheid in the 3-dimensional parameter space classified Cepheid catalog.

TABLE 1

SELECTION CRITERIA FOR THE LIGHT CURVES. P IS THE PERIOD, $m(t)$ THE MAGNITUDE OF THE FOURIER SERIES FIT AT TIME t, $p(t)$ THE POLYNOMIAL FIT AT TIME t AND $y(t)$ IS THE MEASURED MAGNITUDE AT TIME t. THE LAST COLUMN IS THE PERCENTAGE EXCLUDED BY THE CRITERION (IF EACH CRITERION IS APPLIED INDIVIDUALLY) FROM THE 75362 PERIODIC LIGHT CURVES DETECTED BY SIGSPEC.

	Selection criterion			percentage excluded
I	$P_{r_{\mathrm{P1}}}$	$\leq$	75 d	66%
II	$\vert\frac{P_{r_{\mathrm{P1}}}-P_{i_{\mathrm{P1}}}}{P_{r_{\mathrm{P1}}}}\vert$	$<$	0.01	84%
III	$m(t)$	$<$	30 mag	19%
IV	$m(t)$	$>$	15 mag	20%
V	$\int\limits_0^P (m(t)-p(t))^2 dt$	$<$	30	31%
VI	$\max(m(t)) - \min(m(t))$	$\geq$	0.1 mag	4%
VII	$\frac{median(\vert m(t)-y(t)\vert)}{max(m(t))-min(m(t))}$	$\leq$	0.2 mag	42%

a '3-dimensional parameter space' occupied by Cepheids. All variables surviving the selection criteria in Section 4.5 which at the same time reside in the 3-dimensional Cepheid subspace are considered Cepheids as well. The complexity of this 3d subspace is so high that there are no 2d projections that could classify Cepheids as effectively.

We span a $10 \times 10 \times 10$ grid[14] in A_{21}-φ_{21}-P space with $1 \leq \log(P) \leq 75$, $0 \leq A_{21} \leq 0.75$ and $0 \leq \varphi_{21} \leq 2\pi$. We then identify those boxes around the grid-points where the Cepheids of the manually classified subsample reside in. The space defined by those grid-points that have Cepheids around them, defines the 3-dimensional parameter space. The subsample size and the rather large grid span force us to accept grid-points that only have one data point around it. While this is not ideal, the alternative would be to accept only grid-points that have a number of Cepheids above a certain threshold and this would drastically decrease the number of Cepheids at large periods, Type II Cepheids and FO Cepheids.

After the Wesenheit-color cut and the selection criteria are applied there are 2030 light curves within this parameter space, including also those already identified with the manual classification. As stated in Section 3, these light curves can contain RV Tauri light curves. We inspect those 2030 light curves manually and find 21 RV Tauri light curves, which we exclude from the 3-dimensional parameter space classified Cepheid catalog. The final 3-dimensional parameter space classified Cepheid catalog contains 2009 Cepheids (including the 1020 manually classified Cepheids).

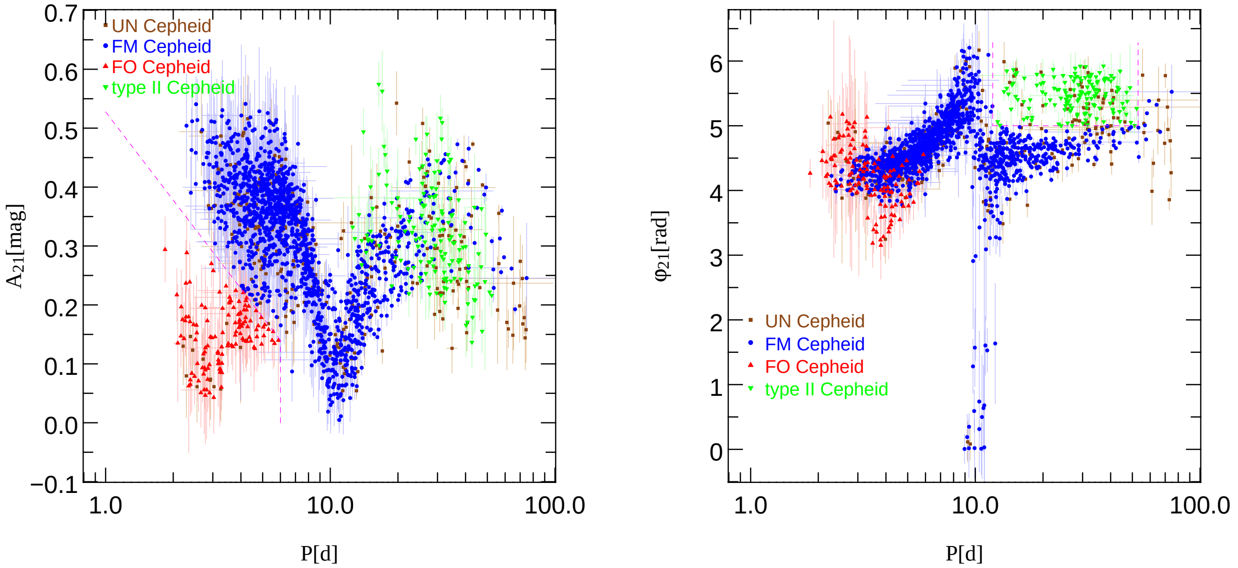

FIG. 9.— 3-dimensional parameter space for the P, A_{21}, φ_{21} 3 dimensional parameter space classified Cepheid catalog in the r_{P1} band. The scopes for the type classification are the same as in Fig. 6. The transitions between the different sequences become more pronounced when compared to those in the manually classified Cepheid catalog, while the shape of the sequences is preserved (c.f. Fig. 6). Left panel: Amplitude ratio A_{21} for the 3-dimensional parameter space classified Cepheid catalog. Right panel: Phase difference φ_{21} for the 3 dimensional parameter space classification.

As can be seen in Fig. 9 the transition region between the different Cepheid types becomes more populated, in

---

[14] A grid with more grid-points could leave gaps, which we want to avoid.

TABLE 2
Excerpt of the 3-dimensional parameter space classified Cepheid catalog. Only a portion of the complete table is shown here. The table in its entirety is available in machine-readable format in the online journal. The columns contain (from left to right): identifier, Cepheid type, RA (J2000.0), DEC (J2000.0), significance (sig), period (determined from the r_{P1} band light curve), mean magnitude in the r_{P1} band, mean magnitude in the i_{P1} band, Fourier coefficient A_{21}, Fourier coefficient φ_{21}, Wesenheit index and the decline/rise factor (c.f. Fig. 21)

identifier	type	RA	DEC	sig	P	r_{P1}	i_{P1}	A_{21}	φ_{21}	W	decl./rise
103-27590	FM	11.1608	42.1585	16.40	4.398	21.34 ± 0.08	21.20 ± 0.08	0.37 ± 0.03	4.37 ± 0.11	20.80 ± 0.38	2.80
040-12157	FM	9.8918	40.4165	16.09	6.304	21.10 ± 0.05	20.92 ± 0.05	0.41 ± 0.03	4.66 ± 0.10	20.40 ± 0.25	2.24
102-03621	FM	11.0967	41.9573	19.07	10.224	20.04 ± 0.02	19.80 ± 0.05	0.19 ± 0.01	4.87 ± 0.07	19.09 ± 0.18	2.14
103-12114	FM	11.3482	42.0301	18.53	10.370	20.73 ± 0.10	20.40 ± 0.10	0.13 ± 0.02	4.32 ± 0.15	19.47 ± 0.48	1.15
064-30826	FM	10.1540	41.2511	32.34	16.563	19.84 ± 0.03	19.63 ± 0.03	0.32 ± 0.01	4.78 ± 0.02	19.02 ± 0.14	1.94
053-14189	FM	10.5470	40.8116	28.07	27.591	19.46 ± 0.02	19.10 ± 0.02	0.44 ± 0.01	4.80 ± 0.02	18.06 ± 0.11	4.38
065-11258	FM	10.2662	41.1512	33.25	45.740	18.78 ± 0.02	18.48 ± 0.04	0.43 ± 0.00	4.89 ± 0.01	17.61 ± 0.15	3.62
090-30644	FM	11.0918	41.9226	18.76	66.429	18.55 ± 0.02	18.20 ± 0.03	0.19 ± 0.01	4.91 ± 0.04	17.21 ± 0.12	1.82
051-15274	FO	9.7241	40.7097	33.30	2.730	21.39 ± 0.08	21.33 ± 0.08	0.08 ± 0.04	4.85 ± 0.44	21.17 ± 0.39	1.14
090-07109	FO	10.6804	41.6543	30.35	3.683	21.23 ± 0.03	20.91 ± 0.05	0.13 ± 0.04	4.35 ± 0.34	20.02 ± 0.20	1.60
041-31081	T2	10.5598	40.5848	29.91	21.514	21.47 ± 0.03	21.23 ± 0.04	0.33 ± 0.03	5.40 ± 0.09	20.56 ± 0.20	3.19
078-12906	T2	10.9476	41.4886	27.59	33.832	20.92 ± 0.05	20.79 ± 0.07	0.44 ± 0.03	5.56 ± 0.07	20.41 ± 0.33	2.01
103-01636	UN	11.4924	41.9421	16.31	5.251	20.39 ± 0.03	20.08 ± 0.05	0.37 ± 0.03	4.14 ± 0.09	19.22 ± 0.19	3.38
077-16136	UN	10.5815	41.4385	28.22	26.096	20.47 ± 0.21	20.08 ± 0.21	0.42 ± 0.01	4.81 ± 0.04	18.98 ± 1.02	4.68

comparison to the manual classified Cepheid catalog (c.f. Fig. 6). This makes the classification of the UN Cepheids with the Period - Wesenheit relation (Fig. 10) even more important. Of the 75362 periodic light curves detected by SigSpec the 3 dimensional parameter space cut alone excludes 94%.

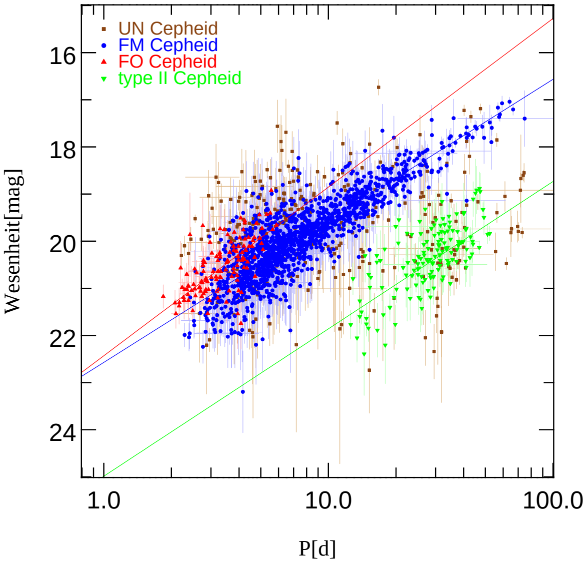

Fig. 10.— Same as Fig. 7, but for the 3-dimensional parameter space classified Cepheid catalog.

It is important to note that while this procedure works well, there are Cepheids that are excluded by this strict 3-dimensional parameter space classification cut. This is due to the grid size and the sampling of the parameter space through the manually classified subsample.

5. THE CATALOG

The 3-dimensional parameter space classified Cepheid catalog contains a total of 2009 Cepheids, consisting of 1440 FM Cepheids, 126 FO Cepheids, 147 Type II Cepheids and 296 UN Cepheids.
Table 2 contains an excerpt of the 3-dimensional parameter space classified Cepheid catalog (the corresponding light curves are shown in Fig. 11, Fig. 12, Fig. 13, Fig. 14, Fig. 15, Fig. 16 and Fig. 17). Table 2 is available in its entirety in machine-readable format in the online journal. A portion is shown here for guidance regarding its form and content.

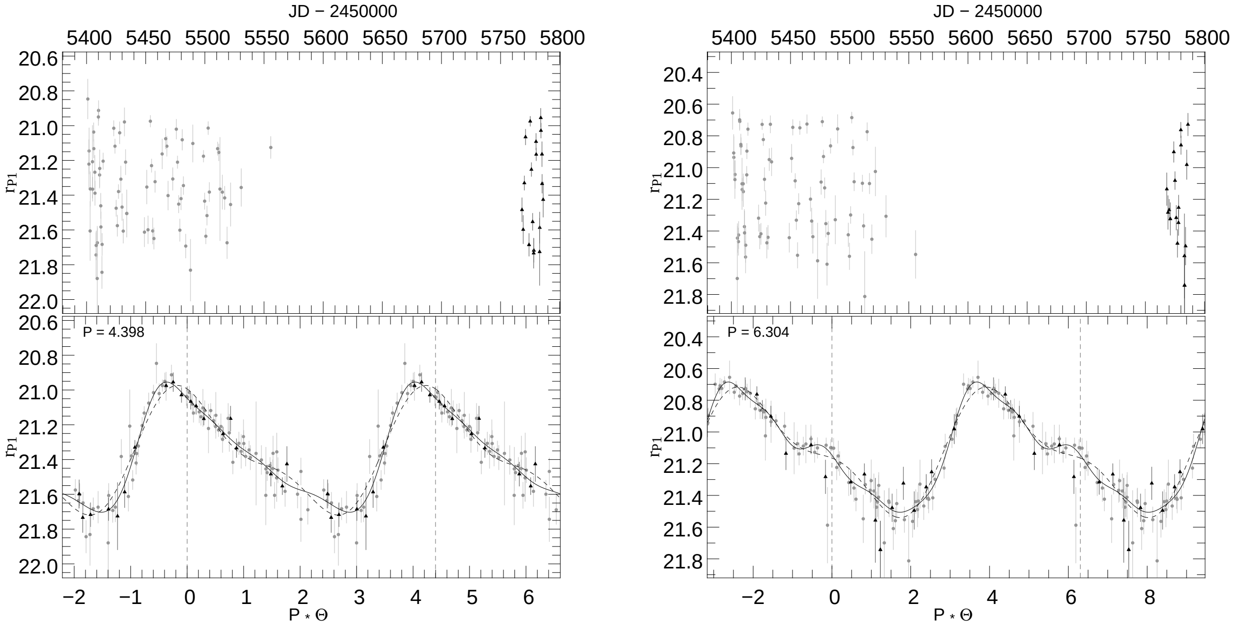

Fig. 11.— Light curves in the r_{P1} band for a part of the excerpt of the 3-dimensional parameter space classified Cepheid catalog. Each top panel shows the unfolded light curve, while each bottom panel shows the variation of the folded light curve over the period times the phase Θ. The folded light curve has been continued in both directions for better illustration, only the middle part between the dashed lines shows the real folded light curve. The grey circle data points represent the 2010 season, while the gray triangle data points are within the 2011 season. The Fourier series fit is the black solid line and the black dashed line represents the light curve that is only defined by A_{21}, φ_{21} and the mean magnitude r_{P1} (c.f. Section 4.1). Left panel: Light curve of a FM Cepheid with $P = 4.398$ d. Right panel: Light curve of a FM Cepheid with $P = 6.304$ d.

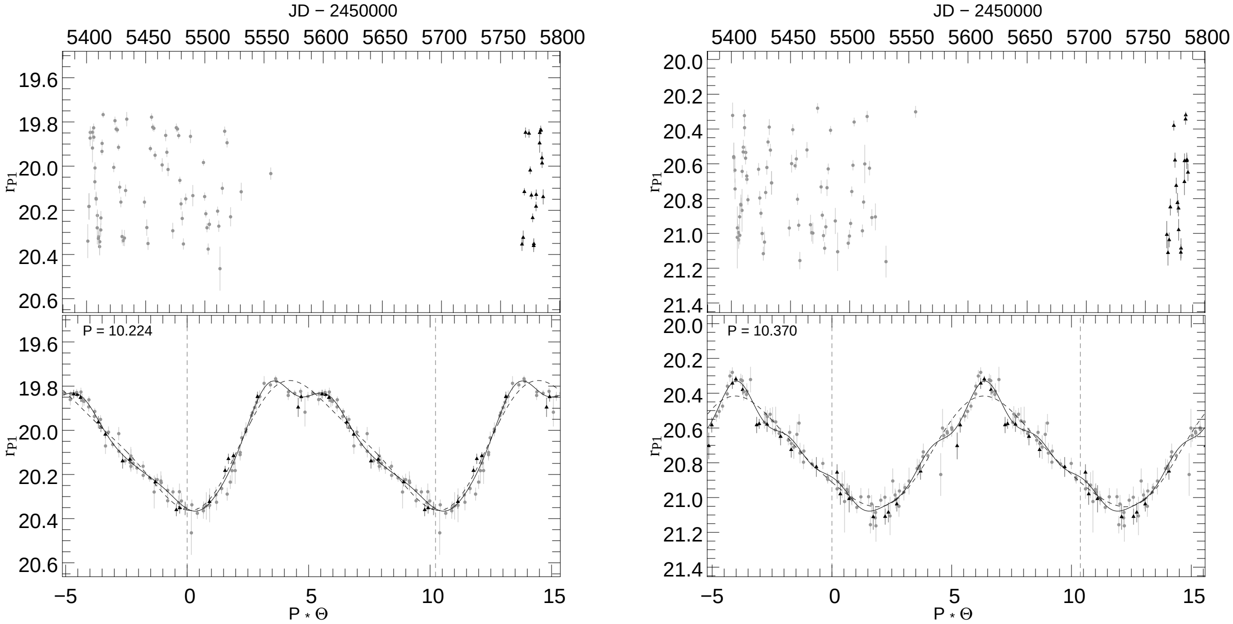

Fig. 12.— Same as Fig. 11 for the next two entries in the excerpt of the 3-dimensional parameter space classified Cepheid catalog. Left panel: Light curve of a FM Cepheid with $P = 10.224$ d. Right panel: Light curve of a FM Cepheid with $P = 10.370$ d.

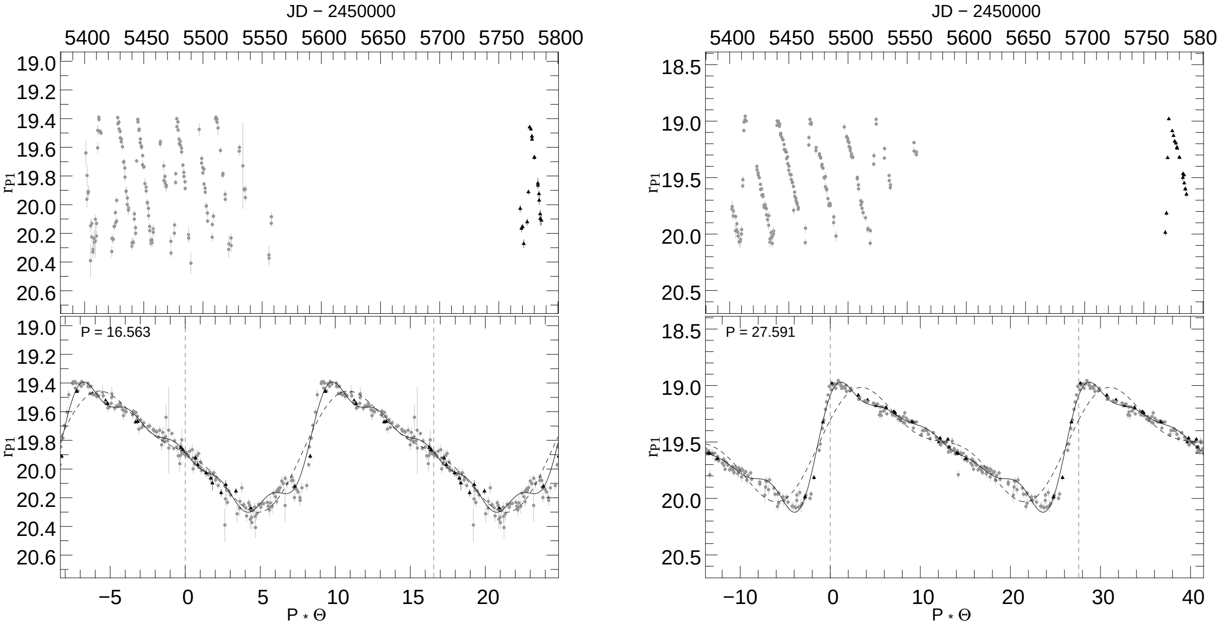

FIG. 13.— Same as Fig. 11 for the next two entries in the excerpt of the 3-dimensional parameter space classified Cepheid catalog. Left panel: Light curve of a FM Cepheid with $P = 16.563$ d. Right panel: Light curve of a FM Cepheid with $P = 27.591$ d.

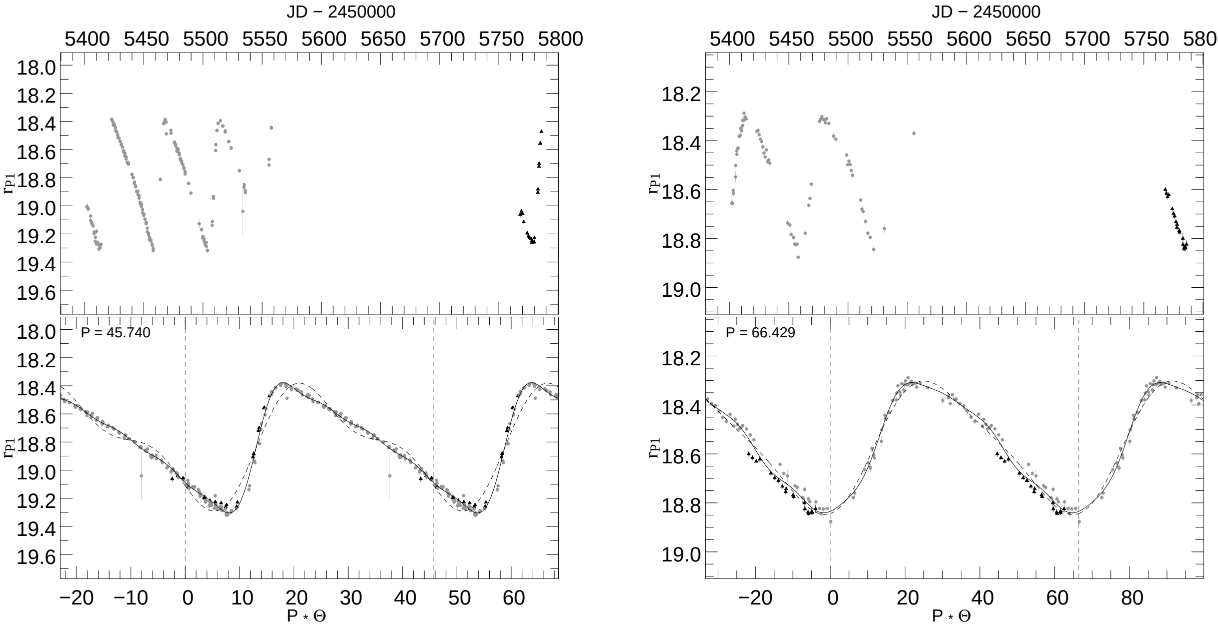

FIG. 14.— Same as Fig. 11 for the next two entries in the excerpt of the 3-dimensional parameter space classified Cepheid catalog. Left panel: Light curve of a FM Cepheid with $P = 45.739$ d. Right panel: Light curve of a FM Cepheid with $P = 66.429$ d.

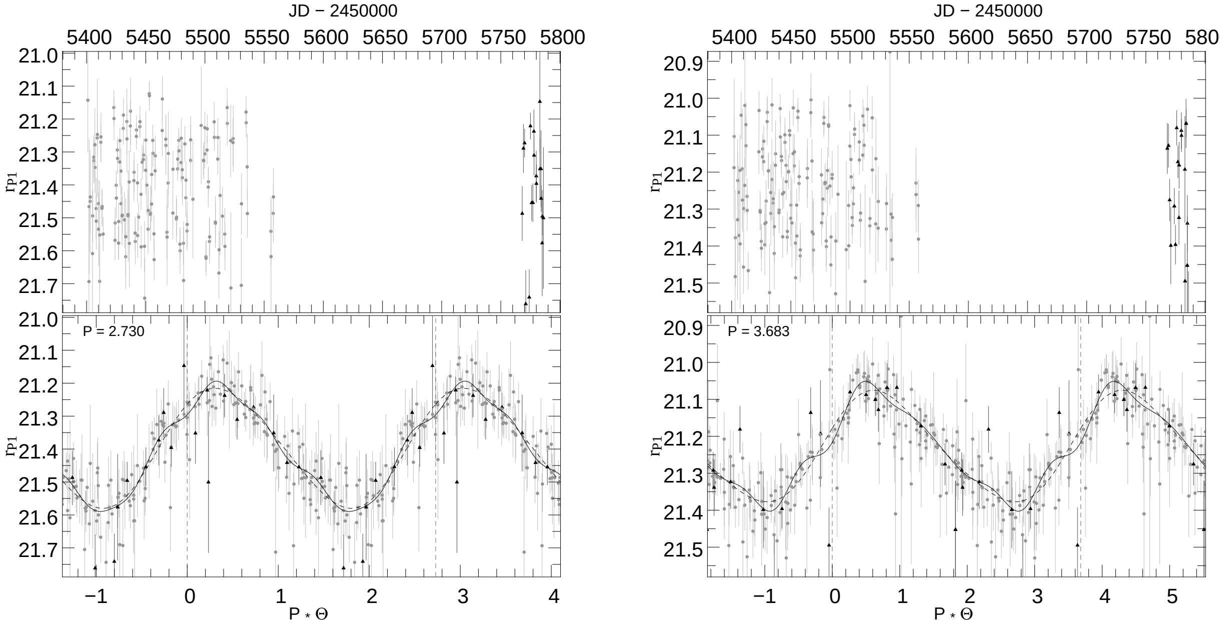

Fig. 15.— Same as Fig. 11 for the next two entries in the excerpt of the 3-dimensional parameter space classified Cepheid catalog. Left panel: Light curve of a FO Cepheid with $P = 2.730$ *d*. Right panel: Light curve of a FO Cepheid with $P = 3.683$ *d*.

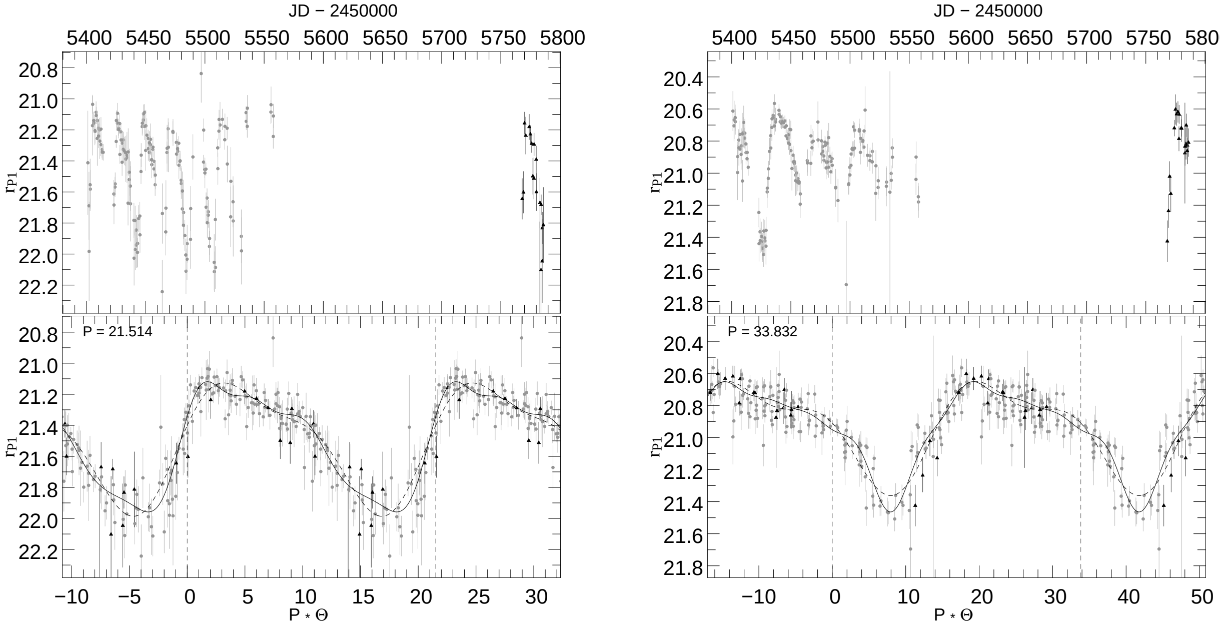

Fig. 16.— Same as Fig. 11 for the next two entries in the excerpt of the 3-dimensional parameter space classified Cepheid catalog. Left panel: Light curve of a Type II Cepheid with $P = 21.513$ *d*. Right panel: Light curve of a Type II Cepheid with $P = 33.831$ *d*.

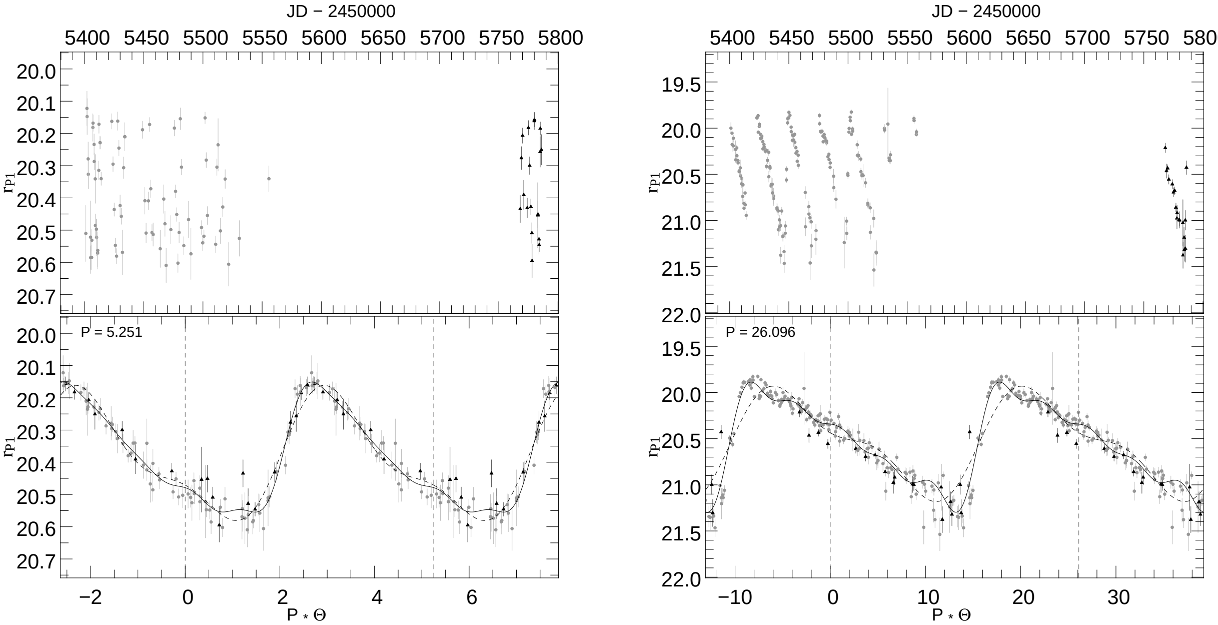

FIG. 17.— Same as Fig. 11 for the next two entries in the excerpt of the 3-dimensional parameter space classified Cepheid catalog. Left panel: Light curve of a UN Cepheid with $P = 5.251\ d$. Right panel: Light curve of a UN Cepheid with $P = 26.095\ d$.

We match the position of the Cepheids in our sample with the 416 Cepheids from Vilardell et al. (2007) and found a coincidence for 225 Cepheids (187 FM, 9 FO, 2 Type II and 27 UN Cepheids) with a matching radius of 1 arcsec. The periods of both samples show a good agreement (Fig. 18). The light curve of the Cepheid with the largest difference in the period (5.101 days) is shown in the right panel of Fig. 16. The reference image shows no other close source and as can be seen from the right panel of Fig. 16 the period determination is reasonable, which suggests a slightly wrong period in the Vilardell sample. The periods for the other 5 light curves with a relative difference larger than 0.5% we were able to confirm by visual inspection, but in some cases we can not rule out that there is another close source within the 1 arcsec matching radius and that the difference is caused by that source.

We also matched our Cepheids with the Cepheids of the DIRECT project (Macri 2004) and the WeCAPP project (Fliri et al. 2006) with the matching radius of 1 arcsec. We found matches for 216 Cepheids from 332 DIRECT Cepheids (187 FM, 3 FO, 0 Type II and 26 UN Cepheids) and 26 matched Cepheids from 126 WeCAPP Cepheids (15 FM, 0 FO, 4 Type II and 7 UN Cepheids). Taking also the Vilardell et al. (2007) sample into account we matched 354 unique Cepheids.

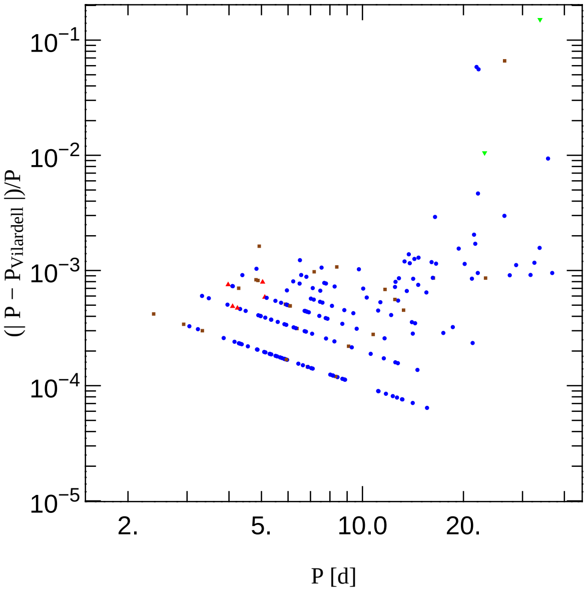

FIG. 18.— Relative difference of our periods with the 225 (187 FM (circles), 9 FO (upwards pointing triangles), 2 Type II (downward pointing triangles) and 27 UN Cepheids (squares)) matched Cepheids from Vilardell et al. (2007). The light curve of the Cepheid with the largest difference in the period is shown in the right panel of Fig. 16. The cascaded form of the relative difference is due to the precision of the compared values.

Fig. 19 shows the color magnitude diagram and the color Wesenheit diagram for all resolved sources in the r_{P1} band and the Cepheids of the 3-dimensional parameter space classified Cepheid catalog. Left panel of Fig. 20 shows the color Wesenheit diagram for the Cepheids alone. We require that the Cepheids lie within the domain enclosed by the dashed line which results from theoretical predictions of the instability strip (see Section 4.2).
Using a simple color cut for the selection of Cepheids would either yield too many interlopers (wide cut) or cut too many Cepheids (narrow cut) as a simple color cut can not account for the tilt of the instability strip in the CMDs (c.f. right panel of 20). The use of the instability strip allows for a strict sample cut and yields a color distribution dominated by Cepheid stars (c.f. left panel of Fig. 20).

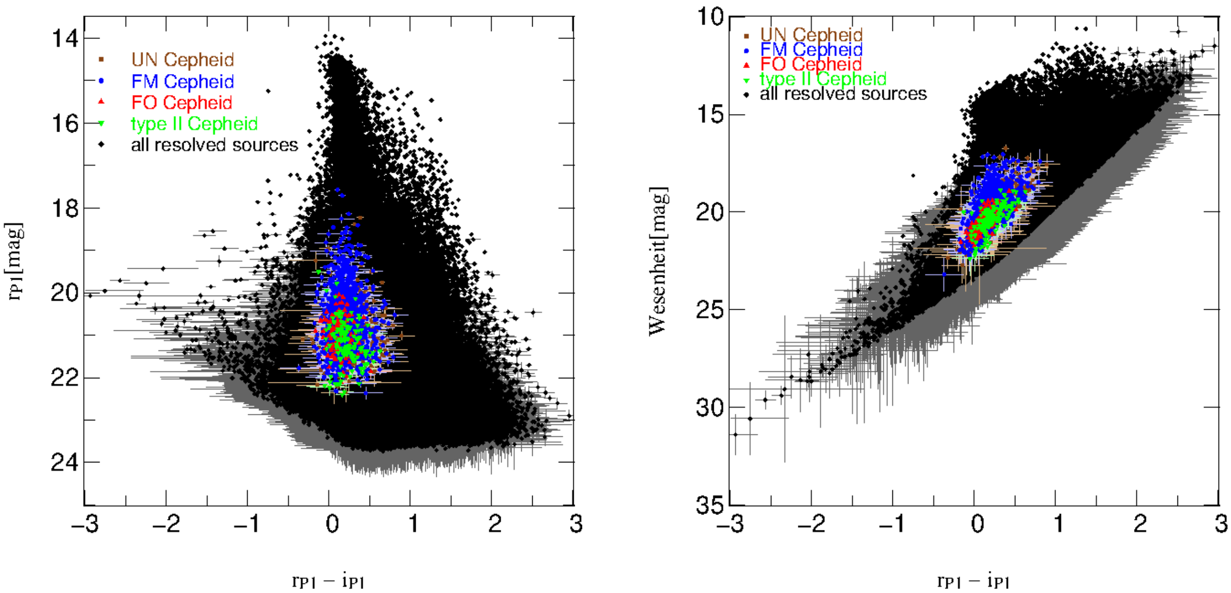

Fig. 19.— Color Wesenheit Diagram and Color Magnitude Diagram for all the 724894 point sources that were detected in the r_{P1} band. Cepheid variable stars are color coded. Left panel: Color Magnitude Diagram. Right panel: Color Wesenheit Diagram.

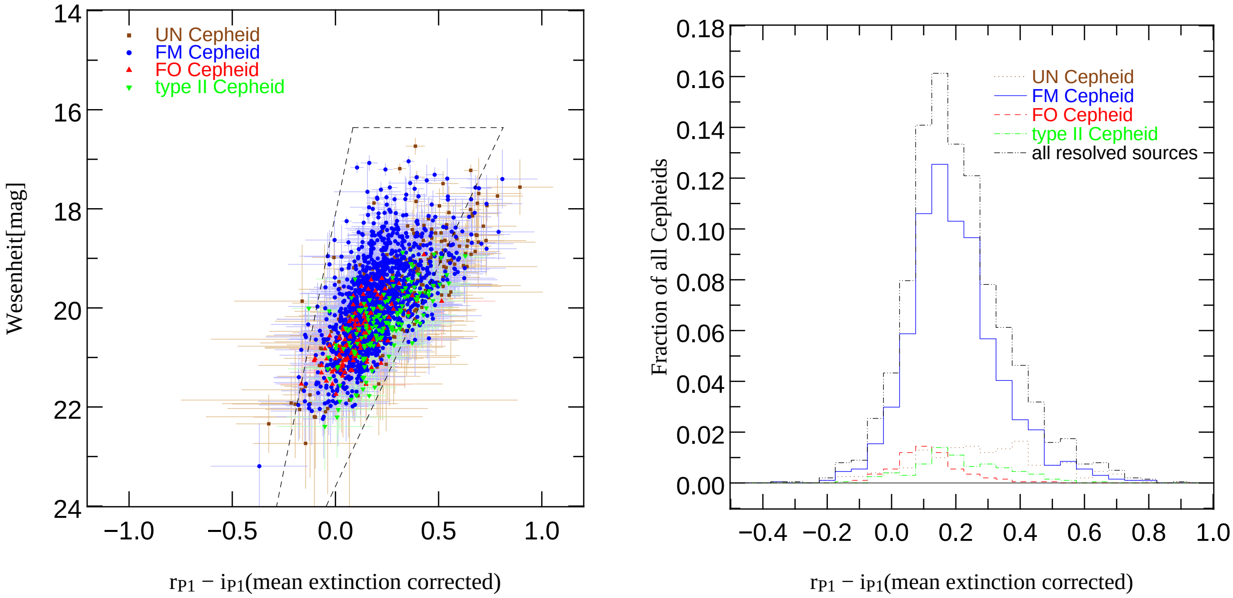

Fig. 20.— Left panel: Color Wesenheit Diagram with the domain (black dashed lines) we require the data points to be in, consistent with their margin of error (c.f. Section 4.2). Right panel: Histogram of the color distribution.

To describe the overall shape of the Cepheid light curve and to trace the bump progression (also known as Hertzsprung progression, Bono et al. 2000) we introduce the decline/rise factor. This factor describes the ratio of the time from the minimal to the maximal magnitude (not flux!) compared to the time from the maximal to the minimal magnitude. Fig. 21 shows that there are different scopes that correspond to the different positions of the bump. Around a period of 10 days two bumps occur on each side of the minimal magnitude and the light curve gets quite symmetrical. This can be verified in our sample light curves in Fig. 12.

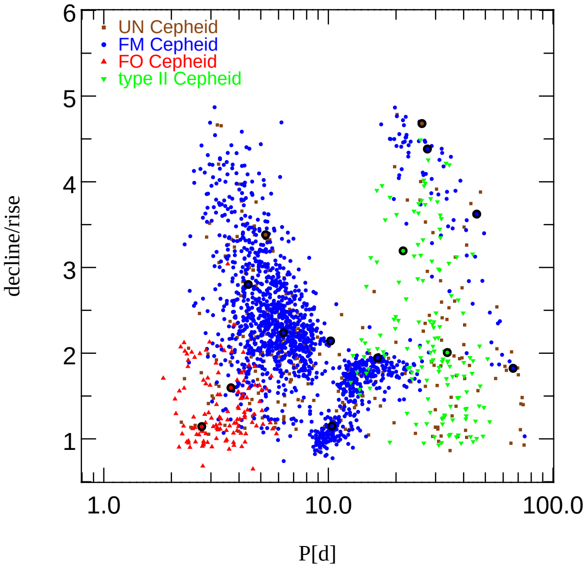

Fig. 21.— Decline/rise factor for the 3-dimensional parameter space classified Cepheid catalog. This factor describes the ratio of the time from the minimal to the maximal magnitude (not flux!) compared to the time from the maximal to the minimal magnitude and it is a good indicator of the overall shape of the light curve. We observe different scopes that correspond to the position of the bump. The 14 Cepheids framed by a black circle are shown in Fig. 11, Fig. 12, Fig. 13, Fig. 14, Fig. 15, Fig. 16 and Fig. 17.

6. RESULTS

So far, the most complete catalog of Cepheid variable stars in M31 had been presented by Vilardell et al. (2007). They found 416 Cepheids of which they classified 281 as FM and 75 as FO objects. We here present a dramatically larger catalog with 2009 candidates, almost 5 times the number of objects in the earlier catalog. The factor ∼ 4.8 difference has to be attributed to the different patrol fields: Vilardell et al. (2007) observed 0.32 square degree within north-eastern lobe of the disk of M31 (and some contribution from bulge and halo) while our Pan-STARRS 1 data cover the full disk, the complete bulge and a large fraction of the M31 halo (only a small part of the halo has been analyzed for this work).

At the distance of M31 (750 to 770 kpc), an arcsecond corresponds to ∼3.7 pc. Therefore, ground-based imaging of individual stars within M31 is subject to blending and crowding, especially for young stars like Type I Cepheids which are often located in young clusters or associations. Even at the resolution of the HST cameras, blending is an issue. The impact of blending has been discussed in detail by Vilardell et al. (2007) for M31 and Chavez et al. (2012) for M33. Chavez et al. (2012) - comparing ground based images to HST images - find severe effects ($\geq$ 10 % level) for more than 30 % of the stars in V and I.

6.1. *FO-to-FM ratio*

Interestingly, the relative amount of FO stars as compared to the FM pulsators differs between Vilardell et al. and our findings, namely, 0.27 vs. 0.09. Both values have their largest uncertainties in the number of unclassified objects as it is rather uncertain to which of the two pulsational modes these objects belong. Incomplete detection can further add uncertainties. As the Vilardell et al. data were obtained with a slightly larger telescope, and with B, V filter bands, they might have a better completeness for the on average bluer and fainter FO stars. Therefore, it is even more puzzling that the FO-to-FM number ratio based on the David Dunlap Observatory Sample (Fernie et al. 1995) of the Milky Way (∼ 0.06) and of the General Calatog of Variable Stars (Samus et al. 2012) within the Milky Way (∼ 0.13) matches nicely our ratio.

We note that the FO-to-FM ratios as derived from the OGLE surveys of the lower metallicity stars forming dwarf galaxies LMC, SMC, and IC 1613 yield ratios in the range 0.4 to 0.7 (see e.g. Udalski et al. 1999b and references therein, and the OGLE project web pages for the catalogs). Comparing these values to the one of the two spiral galaxies might be indicative for a metallicity trend, despite the rather large scatter of the data in this possible relation. FO Cepheids preferentially populate the blue boundary of the instability strip. As isochrones easily demonstrate (see e.g. Fig. 1 in Becker et al. 1977), lower metallicity objects have blue loops in post main sequence evolutions which extend far to the blue and cross the complete strip while higher metalicity shrinks the extent more to the red and the strip is no more fully crossed. Therefore, a trend between host metallicity and FO-to-FM ratio is not surprising.

6.2. *Amplitude ratio*

It is well known that the amplitude of light variations of Cepheids decreases from blue to red wavebands. In several recent investigations of extragalactic samples, the ratio between the amplitudes in two bands has been used to select

Cepheid candidates. We do not use the amplitude ratio for selecting good Cepheid candidates, but derive a ratio between the $r_{\rm P1}$ and $i_{\rm P1}$ of ~ 1.3 with a slight dependence on the period (see Fig. 22 for our M31 sample). This is in excellent agreement with the high quality photometry of galactic Cepheids (FM and FO) by Wisniewski & Johnson (1968). From their light curves we find an average ratio in R and I of 1.28 ± 0.09, and their data points are very well represented by our fit to the M31 sample data (including the slope).

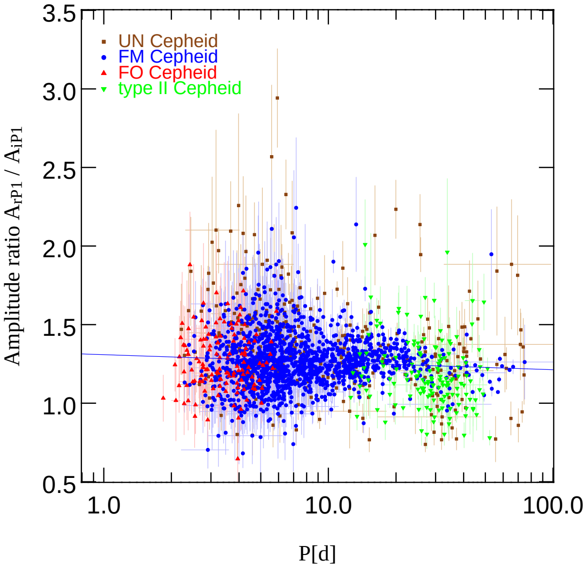

Fig. 22.— Amplitude ratio for the 3-dimensional parameter space classified Cepheid catalog. We observe a slight slope ($A_{r_{\rm P1}}/A_{i_{\rm P1}} = a + b \cdot \log(P)$) with $a = 1.309 \pm 0.006$, $b = -0.0478 \pm 0.0014$ and a dispersion of 0.1680.

6.3. *Period distribution*

The FM period distribution of the presented catalog (Fig. 23) shows a double peaked-distribution with peaks at ~ 0.75 and 1.1 in log(P) (~ 5.5 days and ~ 12.5 days), respectively. The peaks coincide with the ones found previously by Vilardell et al. (2007). Also, the shape of the distribution agrees quite well with the exception that our sample shows a steeper cut-off to the shortest periods which probably is related to the somewhat shallower PS1 data. Thus, our larger data set fully supports the more general finding in the Milky Way and M31 that objects of solar metallicity show a complex period distribution as compared to e.g. the Magellanic Clouds and other low-metal star forming galaxies (Becker et al. 1977, Vilardell et al. 2007, Alcock et al. 1999).

We note that the period distributions of M 101 and NGC 4258, two other large spirals with more than 800 and 300 detected Cepheids, respectively, show similarly double peaked distribution with a local minimum at ~ 10 d (Shappee & Stanek 2011, Macri 2004). Thus, this shape of the distribution seems to be a rather common feature of the Cepheid population of large, solar metallicity spiral galaxies. A full discussion of this topic is beyond the scope of this paper.

6.4. *PL relation*

The Cepheids of the 3-dimensional parameter space classified Cepheid catalog are used to determine the Period-apparent magnitude relations (PL) for the different Cepheid types (Fig. 24). To remove systematic outliers that e.g. result from blending or the wrong extinction correction[15] we additionally perform iterative 3σ clipping (Fig. 25). But in contrast to the 3σ clipping that is used in Section 4.6 for the Period-Wesenheit relation, we use the dispersion of the data points relative to the best fit relation (which we calculate for each iteration step) as an error for each Cepheid magnitude. Otherwise the small errors would result in the elimination of most of the Cepheids, instead of just clipping the systematic outliers. In comparison the use of the dispersion is not necessary for the Period-Wesenheit clipping since the errors in the Wesenheit index are large. The slopes, zero points, the numerical fit errors of these values and the dispersion of the different relations are given in table 3 for a linear fit of the form:

$$m = a \cdot \log(P) + b. \tag{15}$$

For comparison we also added the period-Wesenheit relation from Fig. 10 and the relations for the manually classified Cepheid catalog. The value of the slope a and the values for the intersection b in the usually applied linear approximation of the PLR have been a long standing matter of debate (see Section 1 and literature cited therein). Recently, Freedman & Madore (2011) derived slope values from basic physical principles taking into account the surface temperature and effective surface area. These slope values depend on wavelength (expressed as observing band dependence).

---

[15] Note that as described in Section 4.2 we only correct for the foreground extinction if there is no color excess given in the Montalto et al. (2009) map.

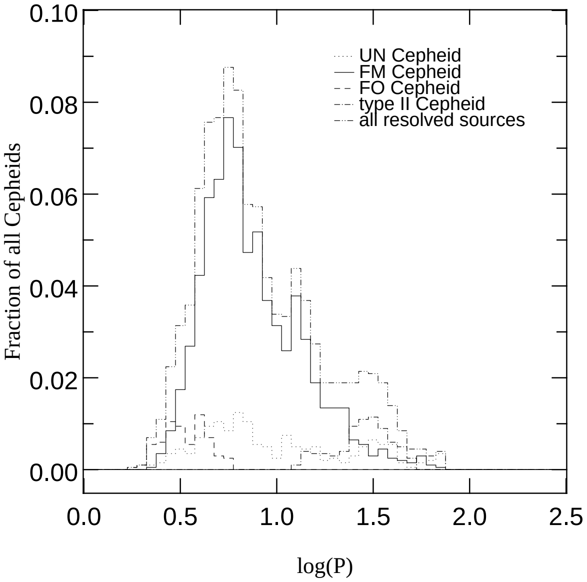

FIG. 23.— Normalized period distribution of the 3-dimensional parameter space classified Cepheid catalog. The period distribution of the FM Cepheids does show a secondary peak as described in Vilardell et al. (2007).

The predictions of Freedman & Madore (2011) agree rather well with empirical values of Fouqué et al. (2007) (Milky Way Cepheids) and of Ngeow & Kanbur (2007) (LMC) including the wavelength dependence. Bono et al. (2010) obtained slope values from pulsation models, but show an underlying relation with a weak additional curvature term (see their Fig. 1). This quadratic behavior is well approximated by a two-slope linear approach with different slope for periods shorter and longer than 10 days (Ngeow et al. 2005, Ngeow et al. 2008) and are in good agreement with the broken slope proposed by Sandage et al. (2009). Bono et al. (2010) provide their slope predictions as a function of metallicity and waveband for short, long and overall period range. Di Criscienzo et al. (2012) obtain slope values similar to Bono et al. (2010) from pulsation models for different period ranges in the SDSS filters. The obtained slopes for $Z = 0.02$ differ from those obtained by Bono et al. (2010).

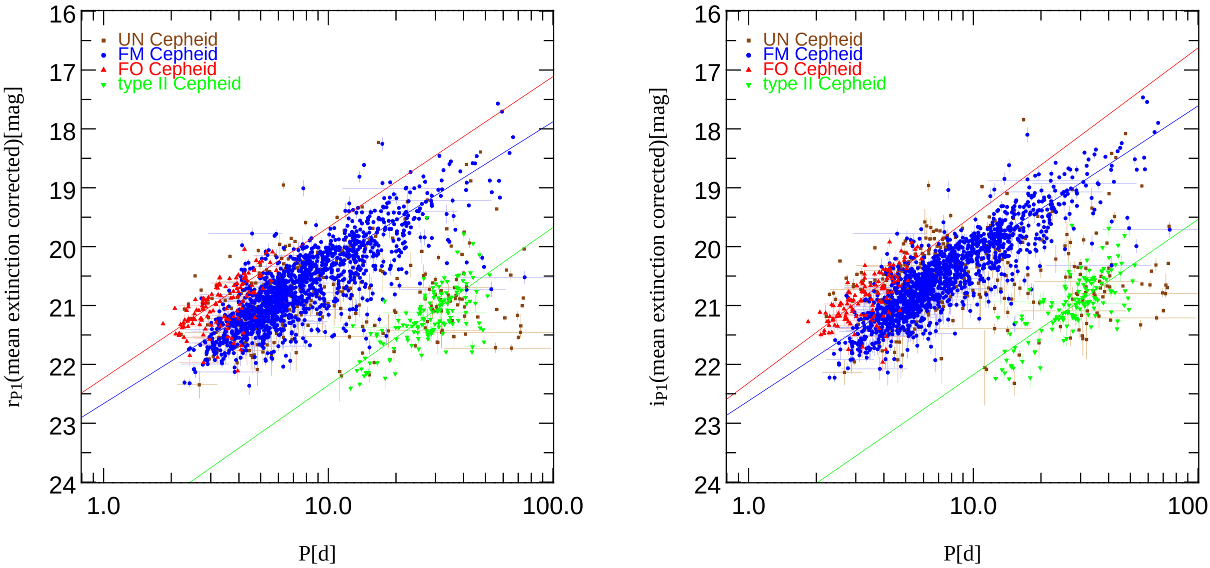

FIG. 24.— Period apparent magnitude relations for the 3-dimensional parameter space classified Cepheid catalog. The according fits shown as solid lines are given in table 3. Left panel: Period apparent magnitude relation in the r_{P1} band. Right panel: Period apparent magnitude relation in the i_{P1} band.

The slope values we derive are surprisingly shallow. In table 3 we also provide slopes for a subsample restricted to Cepheids with periods longer than 10 days. The slopes of the full sample fits in table 3 and those for the subsample with $P > 10\,\mathrm{d}$ yield basically identical values.

As can be seen in Fig. 26 the shallow slope of the subsample with $P > 10\,\mathrm{d}$ agrees with the prediction of Bono et al. (2010) for long periods. This is a warning for applying local PLR's to distant galaxies Cepheid samples which have even shallower (absolute) magnitude limits and are even more dominated by long period Cepheids: The slope values used by Riess et al. (2012) for M31 and by Riess et al. (2011) for 9 more distant hosts perfectly agree with our findings

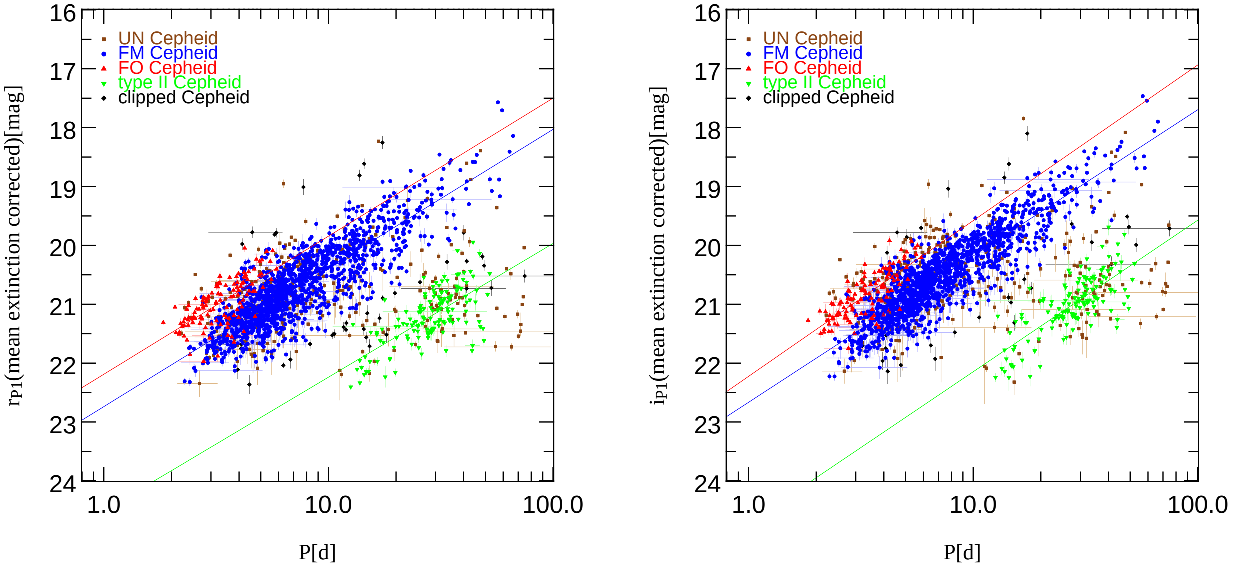

FIG. 25.— Period-apparent magnitude relations with iterative 3σ clipping. For the error bars in the 3σ clipping we use the dispersion of the relation which we calculate for each iteration step. The according fits shown as solid lines are given in table 3. Left panel: Period apparent magnitude relation in the $r_{\rm P1}$ band. Right panel: Period apparent magnitude relation in the $i_{\rm P1}$ band.

and with the predictions of Bono et al. (2010) for long periods. Thus, the effective period range available for a galaxy impacts the derived apparent distance values if the single slope solution for the PL is applied.

TABLE 3
SUMMARY OF THE RESULTS OF THE DIFFERENT PERIOD-APPARENT MAGNITUDE RELATIONS (PL), PERIOD-WESENHEIT RELATIONS (PLW) AND THE PERIOD-APPARENT MAGNITUDE RELATIONS WITH ITERATIVE 3σ CLIPPING. FOR THE ERROR BARS IN THE 3σ CLIPPING (PLC) WE USE THE DISPERSION OF THE RELATION WHICH WE CALCULATE FOR EACH ITERATION STEP. ADDITIONALLY A FIT TO A SUBSAMPLE WITH A PERIOD RESTRICTION (PLP) FOR FM CEPHEIDS IS PROVIDED.

Relation	Catalog	Type	Slope [mag/log(d)]	Zero Point [mag]	Dispersion [mag]
PL ($r_{\rm P1}$ band)	3d	FM	-2.39370 ± 0.00110	22.66600 ± 0.00380	0.42500
PLC ($r_{\rm P1}$ band)	3d	FM	-2.35440 ± 0.00930	22.73900 ± 0.03390	0.35010
PLP ($r_{\rm P1}$ band, P > 10 d)	3d	FM	-2.39060 ± 0.00160	22.66420 ± 0.00980	0.55550
PL ($r_{\rm P1}$ band)	manual	FM	-2.39800 ± 0.00130	22.63410 ± 0.00490	0.40700
PL ($r_{\rm P1}$ band)	3d	FO	-2.56090 ± 0.00370	22.23350 ± 0.01800	0.35040
PLC ($r_{\rm P1}$ band)	3d	FO	-2.34510 ± 0.02650	22.18960 ± 0.12520	0.29360
PL ($r_{\rm P1}$ band)	manual	FO	-2.46520 ± 0.00680	22.14830 ± 0.02920	0.23840
PL ($r_{\rm P1}$ band)	3d	T2	-2.68030 ± 0.00380	25.03480 ± 0.03850	0.38690
PLC ($r_{\rm P1}$ band)	3d	T2	-2.27150 ± 0.02850	24.51130 ± 0.28290	0.34340
PL ($r_{\rm P1}$ band)	manual	T2	-2.40420 ± 0.00720	24.61830 ± 0.06830	0.30380
PL ($i_{\rm P1}$ band)	3d	FM	-2.50490 ± 0.00130	22.61890 ± 0.00470	0.35710
PLC ($i_{\rm P1}$ band)	3d	FM	-2.48490 ± 0.00830	22.66520 ± 0.03000	0.31090
PLP ($i_{\rm P1}$ band, P > 10 d)	3d	FM	-2.43540 ± 0.00190	22.52990 ± 0.01240	0.43030
PL ($i_{\rm P1}$ band)	manual	FM	-2.46910 ± 0.00160	22.55290 ± 0.00610	0.33780
PL ($i_{\rm P1}$ band)	3d	FO	-2.84470 ± 0.00490	22.31370 ± 0.02380	0.31750
PLC ($i_{\rm P1}$ band)	3d	FO	-2.64490 ± 0.02290	22.22470 ± 0.10760	0.25230
PL ($i_{\rm P1}$ band)	manual	FO	-2.94140 ± 0.00840	22.36100 ± 0.04000	0.24290
PL ($i_{\rm P1}$ band)	3d	T2	-2.63900 ± 0.00460	24.81500 ± 0.04680	0.34530
PLC ($i_{\rm P1}$ band)	3d	T2	-2.57460 ± 0.02710	24.72140 ± 0.26840	0.32680
PL ($i_{\rm P1}$ band)	manual	T2	-2.68790 ± 0.00830	24.83940 ± 0.07920	0.30570
PLW	3d	FM	-3.00260 ± 0.00620	22.57140 ± 0.02180	0.44290
PLW	manual	FM	-3.00380 ± 0.00760	22.57660 ± 0.02830	0.40260
PLW	3d	FO	-3.57730 ± 0.02210	22.43020 ± 0.10730	0.41600
PLW	manual	FO	-3.59930 ± 0.03830	22.50680 ± 0.17810	0.39570
PLW	3d	T2	-3.12580 ± 0.02140	24.98560 ± 0.21670	0.51350
PLW	manual	T2	-2.89640 ± 0.03900	24.60340 ± 0.36910	0.49050

In a next step we want to check if our sample is dominated by long period Cepheids. If our sample would be dominated by the long period Cepheids, this would explain why the slopes of our full sample do not agree with the slopes of Bono et al. (2010) for all Cepheids. Therefore we want to compare the slopes of the short period ($P \leq 10\,{\rm d}$) Cepheids to those of the long period Cepheids. Simple linear fits to the short period samples provide almost similar slopes to those of to the long period samples, but with a different zero points. This means that the fits for the different period ranges are not continuous at 10 days. Hence we introduce a different procedure for the fit of the broken slope proposal.

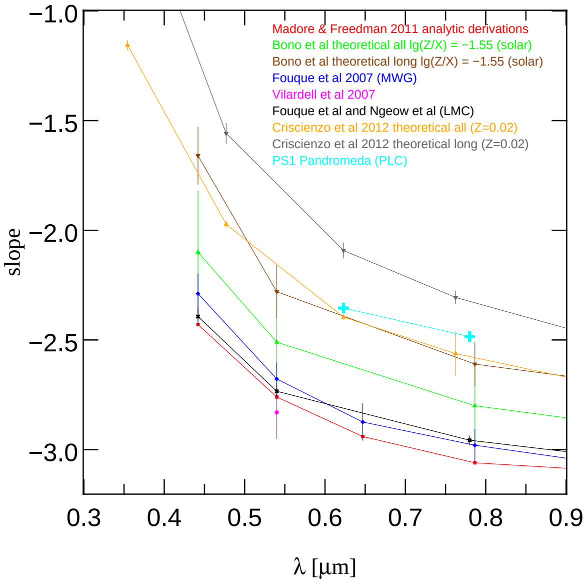

FIG. 26.— PLR slope values as function of wavelength. Our full sample and subsample with $P > 10\,\mathrm{d}$ yield basically identical slopes (color: cyan). They agree with the theoretical predictions of Bono et al. (2010) for long periods (color: brown).

We fit two linear slopes (a_1 and a_2) with a common suspension point (y_{10}) at 10 days ($x_{10} = 10\,\mathrm{d}$):

$$y = a_1 \log(\frac{x}{x_{10}}) + y_{10} \qquad x \leq x_{10} \tag{16}$$

$$y = a_2 \log(\frac{x}{x_{10}}) + y_{10} \qquad x > x_{10} \tag{17}$$

For the FM Cepheids in the r_{P1} band this results in

$$\begin{aligned} y_{10} &= 20.26755 \pm 0.000004 \\ a_1 &= -2.41618 \pm 0.00007 \\ a_2 &= -2.37669 \pm 0.00004 \end{aligned}$$

with a dispersion of 0.36345 for the short periods and a dispersion of 0.55620 for the long periods. This fit is shown in Fig. 27. As can be seen also this fit with a common suspension point does produce similar slopes for the short and long period Cepheids.

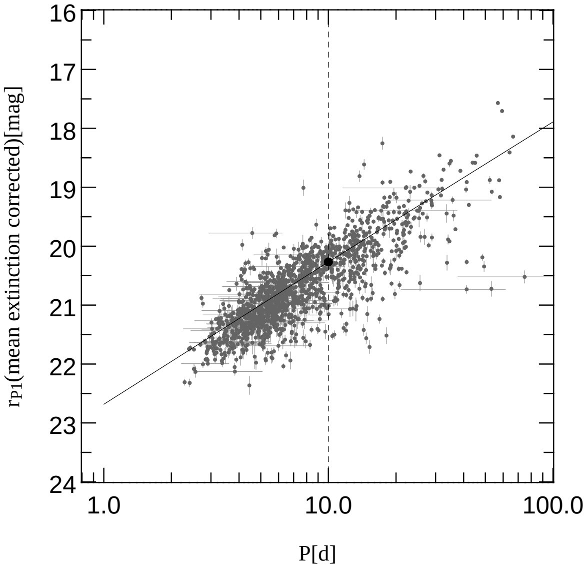

FIG. 27.— Common suspension point fit for FM Cepheids in the r_{P1} band (c.f. equations 16 and 17). The resulting slopes for the short period and long period subsample are very similar.

To check if the dispersion of the PLR is concealing a steeper slope we generate a simulated subsample for the short period Cepheids (in the r_{P1} band) in such a way that the periods of the Cepheids stay the same, but the magnitude is given by a Gaussian distribution around the slope -2.8. The width of the Gaussian distribution is chosen to be the dispersion of the common suspension fit of the short period Cepheids. The subsample of the long period Cepheids stays the same. We generate 100000 Gaussian distributions and perform the common suspension point fit. The resulting distribution of the short period slopes is shown in Fig. 28. As can be seen the shallow slope of the short period subsample cannot be explained by the dispersion of the PLR.

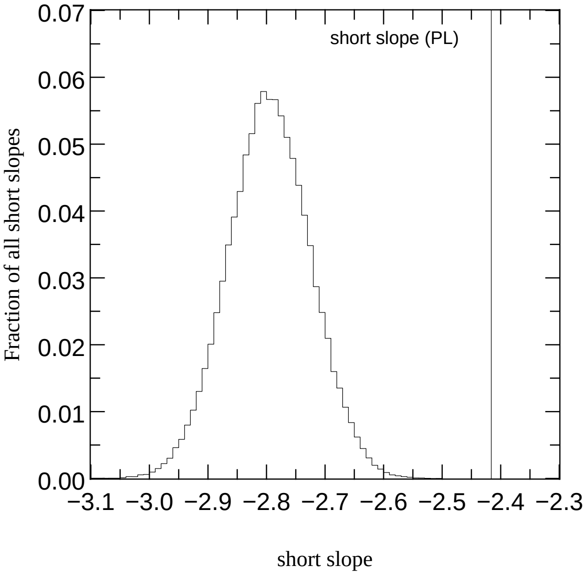

Fig. 28.— Distribution of the period subsample slopes for a Gaussian distribution around the slope -2.8 for the FM Cepheids in the r_{P1} band. The width of the Gaussian distribution is chosen to be the dispersion of the common suspension fit of the short period Cepheids (0.36345). A total of 100000 Gaussian distributions was used to determine the distribution of the short slopes. As can be seen the shallow slope from Fig. 27 cannot be explained by the dispersion of the PLR.

The most likely explanation for the shallow slope at short periods is that we seem to select the brighter Cepheids at short periods due to the Malmquist bias and that most short period Cepheids are too faint to be detected, so that we cannot determine the slope for the short periods correctly. To confirm this we would need to perform completeness tests that are beyond the scope of this work.

Nevertheless the good agreement of our empirical values for the long period Cepheids with the predictions of Bono et al. (2010) supports the finding of Sandage et al. (2009) of a different slope for long and short period Cepheids, depending on the observational band, and the more general prediction of a curvature term in the PLR.

6.5. *Spatial Cepheid distribution*

We now investigate the location of the Cepheids in the M31 plane. Fig. 29 shows the position of the Cepheids plotted over the E(B-V) map of Montalto et al. (2009). The FM and FO Cepheids are concentrated towards the disk and clearly show a ring like structure (left panel in Fig. 29), while the older Type II Cepheids trace the halo of M31 (right panel in Fig. 29). Fig. 30 shows a contour plot of the distribution of the Cepheids. While we can see the same behavior of the FM and FO Cepheids as in Fig. 29, we observe that the Type II distribution is limited by the area of the skycells that were analyzed. For the next data release we will increase this area so as to better trace the halo. We do not discuss the spatial distribution of Cepheids around NGC 206 but refer the reader to Magnier et al. (1997).

6.6. *Spatial age distribution*

The spatial distribution of FM and FO Cepheids can be used to obtain a spatial age distribution for M31. We use the period-age relation for FM and FO Cepheids given by Bono et al. (2005) to determine the age of each Cepheid. The spatial age distribution shown in Fig. 31 indicates that star formation in the last $\sim$ 100 Myr was concentrated in a ring which is in good agreement with Davidge et al. (2012). Fig. 31 also hints a correlation between the Cepheid age and the distance to the center of M31.

In order to check for this correlation we deproject the spatial distribution. We use 75° for the inclination and 37° for the tilt angle and the radius and offset of the 10 kpc ring given by Gordon et al. (2006). The deprojected age map is shown in Fig. 32. We found the splitting of the ring as previously described in Gordon et al. (2006). Gordon et al. (2006) attributes the star formation of the ring and its splitting to a passage of M32 through the M31 disk. In a next step we analyze the age of the Cepheids as a function of distance to the 10 kpc ring. For this analysis we exclude all Cepheids in the splitted part of the ring ($150 \leq \varphi \leq 260$, c.f. right panel in Fig. 32). Fig. 33 shows the median Cepheid age as a function of the distance to the 10 kpc ring in bins of 0.5 deg. The first and the last two bins contain less than 10 Cepheids and can therefore be neglected. The errors in each bin have been determined with the bootstrap method (c.f. Section 3) and are rather small compared to the dispersion in the bins we consider. The upper left corner

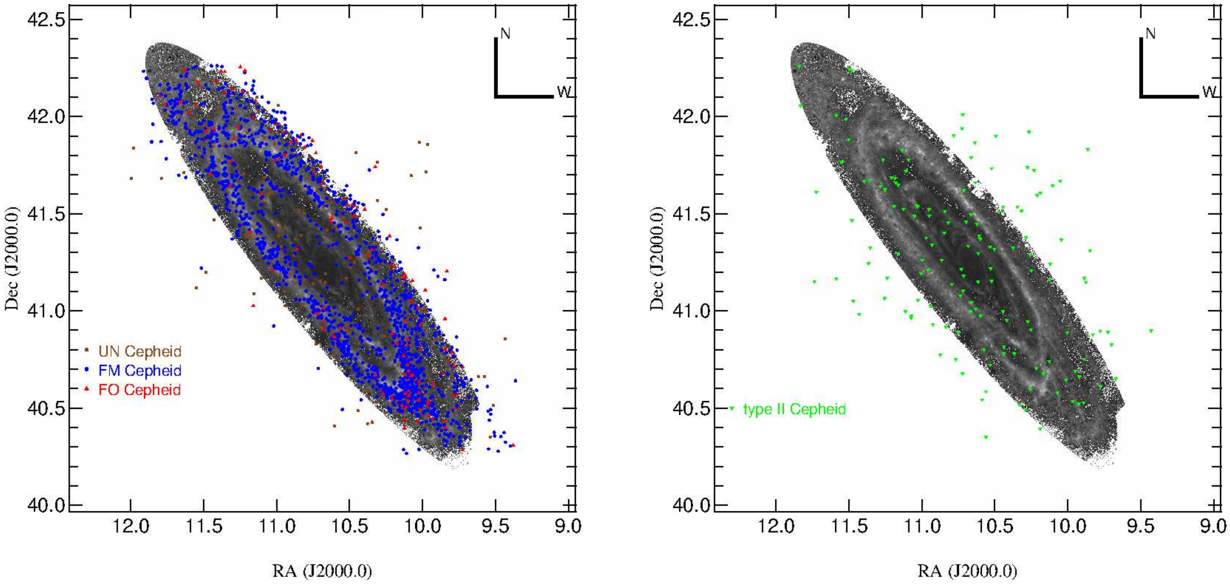

FIG. 29.— RA-Dec of the 3-dimensional parameter space classified Cepheid catalog, plotted over the E(B-V) map of Montalto et al. (2009). It can clearly be seen that the FM and FO Cepheids trace the spiral arms, while the Type II Cepheids trace the M31 halo. Left panel: FM and FO Cepheid distribution. Right panel: Type II Cepheid distribution.

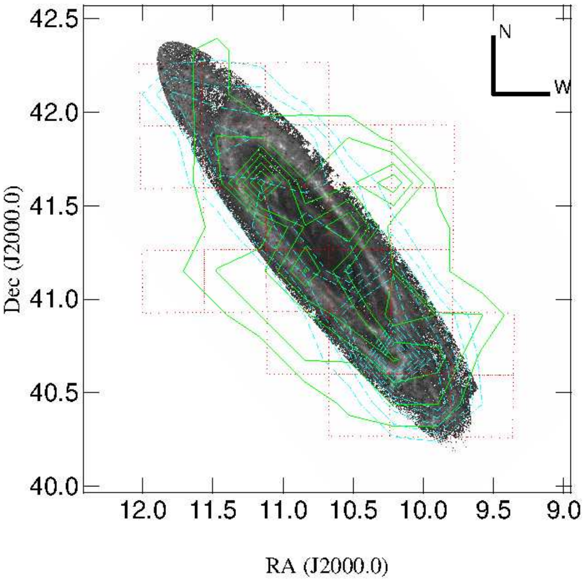

FIG. 30.— Contour plot of the RA-Dec distribution for the 3-dimensional parameter space classified Cepheid catalog, plotted over the E(B-V) map of Montalto et al. (2009). It can be seen that the FM and FO distribution (cyan dashed lines) follows the spiral arms, while the Type II distribution (green solid lines) traces the M31 halo. The Type II distribution is limited by the skycells (red dotted lines) that were analyzed until now. The ten contour line levels represent 1% - 10% of the respective Cepheid type number. For the FM and FO distribution this number is the total number of FM and FO combined.

of the upper panel of Fig. 33 contains no Cepheids. In this region (the center of M31) the signal to noise ratio is low, so that this is likely the reason that we hardly detect faint Cepheids (i.e. Cepheids with small periods; the study of the detection efficiency for Cepheids will be subject of a further work) and thus we hardly detect old Cepheids in this region. In the seventh bin we detect old (faint) Cepheids but no young Cepheids, although they should be more easily detectable than old Cepheids. Therefore the lack of young Cepheids in the outer region of the ring is no selection bias. This leaves us with the conclusion that the age gradient is real. To measure the strength of the age gradient we perform a fit to the median age with $y = a + b \cdot x$:

$$a = 55.4941 \pm 0.7692 \; [Myr]$$
$$b = 33.8517 \pm 0.6100 \; [Myr/deg]$$

with a $\frac{\Delta\chi^2}{\mathrm{d.o.f.}} = 0.36$. We therefore conclude that the median age of the stellar population decreases by $\sim 34 \; Myr/deg$ inwards. A possible interpretation for this is that the star formation is related to the interaction with M32 moving inwards.

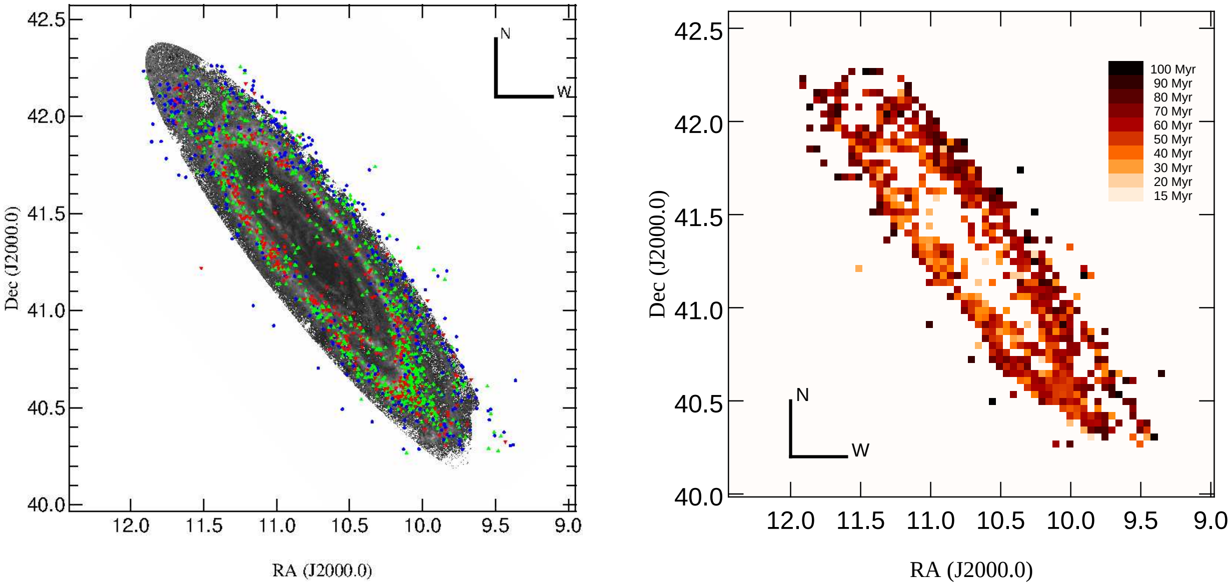

FIG. 31.— Spatial age distribution for the 3-dimensional parameter space classified Cepheid catalog for different Cepheid ages, plotted over the E(B-V) map of Montalto et al. (2009). To calculate the age we use the period-age relations from Bono et al. (2005). The spatial age distribution shows that the star formation in last $\sim$ 100 Myr was concentrated in a ring, which is in good agreement with Davidge et al. (2012). Blue points: FM and FO Cepheids with $t \geq 70$ Myr; Green upward pointing triangle: FM and FO Cepheids with 70 $Myr > t \geq 40$ Myr; Red downward pointing triangle: $t < 40$ Myr. Left panel: RA-Dec distribution. Right panel: RA-Dec distribution with the median age for each bin.

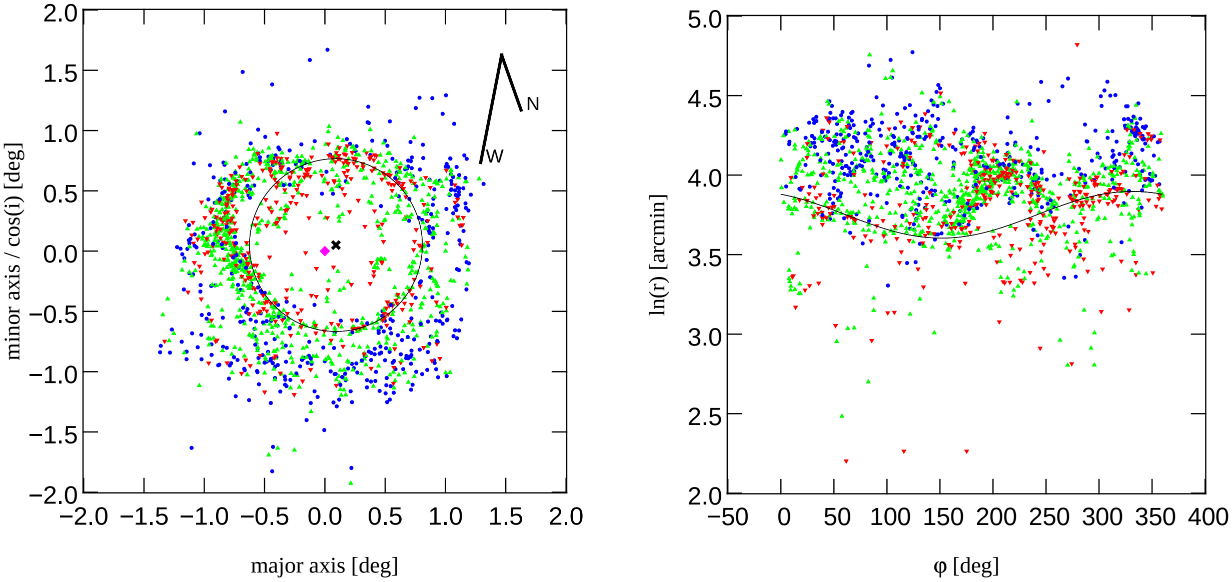

FIG. 32.— Deprojected spatial age distribution for the 3-dimensional parameter space classified Cepheid catalog. To calculate the age we use the period-age relations from Bono et al. (2005). The ring and the splitting of the ring near M32 have been discussed in Gordon et al. (2006).It can be seen that the star formation is clustered at the 10 kpc ring (Davidge et al. 2012). Blue points: FM and FO Cepheids with $t \geq 70$ Myr; Green upward pointing triangle: FM and FO Cepheids with 70 $Myr > t \geq 40$ Myr; Red downward pointing triangle: $t < 40$ Myr, black solid line: 10 kpc ring from Gordon et al. (2006) (the center of the ring is the black cross and the magenta point the center of M31). Left panel: Deprojected age map. Right panel: Deprojected age map in polar coordinates.

7. CONCLUSION AND OUTLOOK

We present a large sample of Cepheids in M31 in the $r_{\rm P1}$ and $i_{\rm P1}$ filters. We develop an automatic Cepheid detection and classification scheme based on the Fourier parameters P, A_{21} and φ_{21} and the location of the instability strip in the Wesenheit-color plane. This makes the Cepheid detection and classification less biased than traditional methods and facilitates Cepheid detection in large surveys.

We find 1440 fundamental mode (FM) Cepheids, 126 Cepheids in the first overtone mode (FO), 147 belonging to the Population II types and 296 Cepheids that could not be classified. 354 of the 2009 Cepheids could be found in other surveys (Vilardell et al. 2007, Fliri et al. 2006 and the DIRECT project, Macri 2004) with a matching radius of 1 arcsec. The matching tables are provided in electronical form.

The spatial distribution of FM and FO Cepheids follows the 10 kpc ring in M31, while the Type II Cepheids are

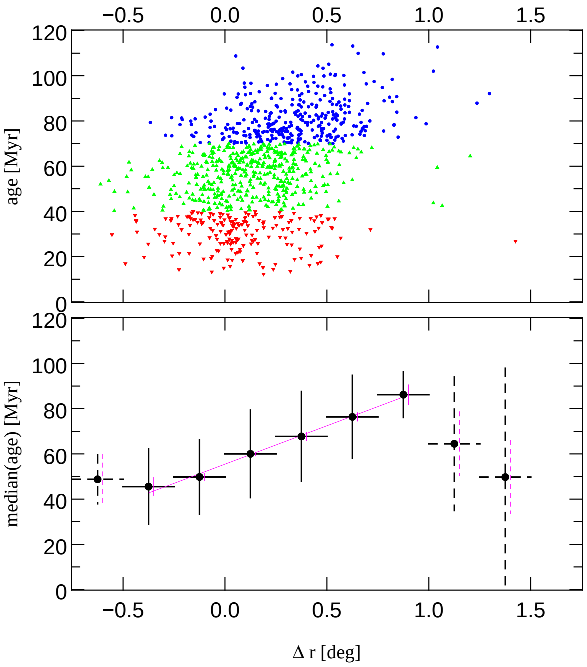

Fig. 33.— Age distribution as a function of distance to the 10 kpc ring. The definition of the symbols and colors is the same as in Fig. 32. The splitted part of the ring ($150 \leq \varphi \leq 260$, c.f. right panel in Fig. 32) was excluded. In the top panel the age distribution for the FM and FO Cepheids can be seen. The bottom panel shows the median age for bins with width of 0.5 deg. The first and the last two bins contain less than 10 Cepheids and thus can be neglected. The errors of the medians have been determined with the bootstrap method (c.f. Section 3). The errors determined with the bootstrap method are shown in magenta with an offset of 0.025 deg for better visibility. The dispersion of each bin is shown in black. We observe an age gradient and the fit to the median age ($y = a + b \cdot x$) is shown as a solid magenta line. The age gradient suggests that the star formation related to the interaction to M32 moved inwards. No Cepheids can be found in the top left corner of the upper panel (the center of M31). We hardly detect old (faint) Cepheids in this region, most likely due to the low signal to noise ratio in the center of M31. The lack of young Cepheids in the outer region of the ring is no selection bias, since we detect old (faint) Cepheids in the seventh bin, but no young Cepheids, although they should be more easily detectable than old Cepheids. This leaves us with the conclusion that the age gradient is real.

distributed throughout the halo of M31. The spatial age distribution shows a positive age gradient with increasing distance from the 10 kpc ring, which implies that the star formation in the 10 kpc ring moved inwards.

The analysis of our period luminosity relations (PLR) indicates that the PLR is slightly curved. This has ramifications on the determination of extra galactic distances, since most of the commonly used calibrations of the PLR are dominated by the short period Cepheids and the typical Cepheids that are used for the extra galactic distance determination are long period Cepheids.

The next data release will cover more area of the M31 halo, thus we will be able to trace the halo better. With another year of observations we will be able to extend the sample to larger periods. Overlapping skycells will improve the calibration and enable completeness tests.

The complete catalog of the 2009 Cepheids can be found electronically in the CDS database.

We acknowledge the careful reading and helpful comments by the anonymous referee. The Pan-STARRS1 Surveys (PS1) have been made possible through contributions of the Institute for Astronomy, the University of Hawaii, the Pan-STARRS Project Office, the Max-Planck Society and its participating institutes, the Max Planck Institute for Astronomy, Heidelberg and the Max Planck Institute for Extraterrestrial Physics, Garching, The Johns Hopkins University, Durham University, the University of Edinburgh, Queen's University Belfast, the Harvard-Smithsonian Center for Astrophysics, the Las Cumbres Observatory Global Telescope Network Incorporated, the National Central University of Taiwan, the Space Telescope Science Institute, and the National Aeronautics and Space Administration under Grant No. NNX08AR22G issued through the Planetary Science Division of the NASA Science Mission Directorate. This research was supported by the DFG cluster of excellence Origin and Structure of the Universe (www.universe-cluster.de).

REFERENCES

Abazajian, K. N., Adelman-McCarthy, J. K., Agüeros, M. A., et al. 2009, ApJS, 182, 543
Alard, C., & Lupton, R. H. 1998, ApJ, 503, 325
Alcock, C., Allsman, R. A., Alves, D. R., et al. 1999, AJ, 117, 920
Baade, W., & Swope, H. H. 1965, AJ, 70, 212
Becker, S. A., Iben, Jr., I., & Tuggle, R. S. 1977, ApJ, 218, 633
Bertin, E., & Arnouts, S. 1996, A&AS, 117, 393
Bono, G., Caputo, F., Marconi, M., & Musella, I. 2010, ApJ, 715, 277
Bono, G., Marconi, M., Cassisi, S., et al. 2005, ApJ, 621, 966
Bono, G., Marconi, M., & Stellingwerf, R. F. 2000, A&A, 360, 245
Chavez, J. M., Macri, L. M., & Pellerin, A. 2012, AJ, 144, 113
Davidge, T. J., McConnachie, A. W., Fardal, M. A., et al. 2012, ApJ, 751, 74
Deb, S., & Singh, H. P. 2009, A&A, 507, 1729

Di Criscienzo, M., Marconi, M., Musella, I., Cignoni, M., & Ripepi, V. 2012, ArXiv e-prints

Fernie, J. D., Evans, N. R., Beattie, B., & Seager, S. 1995, Information Bulletin on Variable Stars, 4148, 1

Fiorentino, G., Caputo, F., Marconi, M., & Musella, I. 2002, ApJ, 576, 402

Fiorentino, G., Marconi, M., Musella, I., & Caputo, F. 2007, A&A, 476, 863

Fliri, J., Riffeser, A., Seitz, S., & Bender, R. 2006, A&A, 445, 423

Fouqué, P., Arriagada, P., Storm, J., et al. 2007, A&A, 476, 73

Freedman, W. L., & Madore, B. F. 2011, ApJ, 734, 46

Freedman, W. L., Madore, B. F., Gibson, B. K., et al. 2001, ApJ, 553, 47

Gerke, J. R., Kochanek, C. S., Prieto, J. L., Stanek, K. Z., & Macri, L. M. 2011, ApJ, 743, 176

Girardi, L., Williams, B. F., Gilbert, K. M., et al. 2010, ApJ, 724, 1030

Gordon, K. D., Bailin, J., Engelbracht, C. W., et al. 2006, ApJ, 638, L87

Hodapp, K. W., Kaiser, N., Aussel, H., et al. 2004, Astronomische Nachrichten, 325, 636

Hubble, E. P. 1929, ApJ, 69, 103

Johnson, L. C., Seth, A. C., Dalcanton, J. J., et al. 2012, ApJ, 752, 95

Kaiser, N., Aussel, H., Burke, B. E., et al. 2002, in Society of Photo-Optical Instrumentation Engineers (SPIE) Conference Series, Vol. 4836, Society of Photo-Optical Instrumentation Engineers (SPIE) Conference Series, ed. J. A. Tyson & S. Wolff, 154–164

Koppenhoefer, J., Saglia, R. P., & Riffeser, A. 2011, Experimental Astronomy, 141

Leavitt, H. S. 1908, Annals of Harvard College Observatory, 60, 87

Leavitt, H. S., & Pickering, E. C. 1912, Harvard College Observatory Circular, 173, 1

Lee, C.-H., Riffeser, A., Koppenhoefer, J., et al. 2012, AJ, 143, 89

Lomb, N. R. 1976, Ap&SS, 39, 447

Macri, L. M. 2004, in Astronomical Society of the Pacific Conference Series, Vol. 310, IAU Colloq. 193: Variable Stars in the Local Group, ed. D. W. Kurtz & K. R. Pollard, 33

Madore, B. F. 1976, MNRAS, 177, 215

—. 1982, ApJ, 253, 575

Magnier, E. 2006, in The Advanced Maui Optical and Space Surveillance Technologies Conference

Magnier, E. A., Prins, S., Augusteijn, T., van Paradijs, J., & Lewin, W. H. G. 1997, A&A, 326, 442

Majaess, D., Turner, D., & Gieren, W. 2011, ApJ, 741, L36

Marigo, P., Girardi, L., Bressan, A., et al. 2008, A&A, 482, 883

Montalto, M., Seitz, S., Riffeser, A., et al. 2009, A&A, 507, 283

Ngeow, C., & Kanbur, S. M. 2007, ApJ, 667, 35

Ngeow, C., Kanbur, S. M., & Nanthakumar, A. 2008, A&A, 477, 621

Ngeow, C.-C., Kanbur, S. M., Nikolaev, S., et al. 2005, MNRAS, 363, 831

Opolski, A. 1983, Information Bulletin on Variable Stars, 2425, 1

Reegen, P. 2007, A&A, 467, 1353

Riess, A. G., Fliri, J., & Valls-Gabaud, D. 2012, ApJ, 745, 156

Riess, A. G., Macri, L., Casertano, S., et al. 2011, ApJ, 730, 119

Riffeser, A. 2006

Riffeser, A., Fliri, J., Gössl, C. A., et al. 2001, A&A, 379, 362

Samus, N. N., Durlevich, O. V., Kireeva, N., et al. 2012

Sandage, A., & Tammann, G. A. 2008, ApJ, 686, 779

Sandage, A., Tammann, G. A., & Reindl, B. 2009, A&A, 493, 471

Scargle, J. D. 1982, ApJ, 263, 835

Schlafly, E. F., & Finkbeiner, D. P. 2011, ApJ, 737, 103

Schlegel, D. J., Finkbeiner, D. P., & Davis, M. 1998, ApJ, 500, 525

Shappee, B. J., & Stanek, K. Z. 2011, ApJ, 733, 124

Sterken, C., & Jaschek, C. 2005, Light Curves of Variable Stars: A Pictorial Atlas (Cambridge University Press)

Tomaney, A. B., & Crotts, A. P. S. 1996, AJ, 112, 2872

Tonry, J., & Onaka, P. 2009, in Advanced Maui Optical and Space Surveillance Technologies Conference,

Tonry, J. L., Stubbs, C. W., Lykke, K. R., et al. 2012, ArXiv e-prints

Udalski, A., Soszynski, I., Szymanski, M., et al. 1999a, Acta Astron., 49, 223

—. 1999b, Acta Astron., 49, 437

Udalski, A., Szymanski, M., Kubiak, M., et al. 1999c, Acta Astron., 49, 201

Valentijn, E. A., McFarland, J. P., Snigula, J., et al. 2007, in Astronomical Society of the Pacific Conference Series, Vol. 376, Astronomical Data Analysis Software and Systems XVI, ed. R. A. Shaw, F. Hill, & D. J. Bell, 491

Vilardell, F., Jordi, C., & Ribas, I. 2007, A&A, 473, 847

Vilardell, F., Ribas, I., & Jordi, C. 2006, A&A, 459, 321

Vilardell, F., Ribas, I., Jordi, C., et al. 2010, in Astronomical Society of the Pacific Conference Series, Vol. 435, Binaries - Key to Comprehension of the Universe, ed. A. Prša & M. Zejda, 375

Wisniewski, W. Z., & Johnson, H. L. 1968, Communications of the Lunar and Planetary Laboratory, 7, 57